

The sub-arcsecond ILT view of the Boötes Deep Field: A link between low-frequency kiloparsec radio morphology and AGN driven ionised outflows

Emmy L. Escott^{1,2*}, Leah K. Morabito^{1,3}, Frits Sweijen¹, Chris M. Harrison⁴, James Petley⁵, Jurjen M. G. H. J. de Jong^{5,6}, Reinout J. van Weeren⁵, Thomas S. Higginson⁷, Isabella Prandoni⁸, George Miley⁵, Huub J. A. Röttgering⁵

¹Centre for Extragalactic Astronomy, Department of Physics, Durham University, Durham DH1 3LE, UK

²Australia Telescope National Facility, CSIRO, Space and Astronomy, PO Box 1130, Bentley, WA 6102, Australia

³Institute for Computational Cosmology, Department of Physics, University of Durham, South Road, Durham DH1 3LE, UK

⁴School of Mathematics, Statistics and Physics, Newcastle University, NE1 7RU, UK

⁵Leiden Observatory, Leiden University, PO Box 9513, 2300 RA Leiden, The Netherlands

⁶ASTRON, The Netherlands Institute for Radio Astronomy, Postbus 2, 7990 AA Dwingeloo, The Netherlands

⁷School of Physics, University of Bristol, HH Wills Physics Laboratory, Tyndall Avenue, Bristol BS8 1TL, UK

⁸INAF-IRA, Via P. Gobetti 101, 40129 Bologna, Italy

Accepted 2026 February 03. Received 2026 January 29; in original form 2025 August 29

ABSTRACT

Active Galactic Nuclei (AGN) outflows can regulate host galaxy evolution via AGN feedback. Ionised gas outflows have been linked to enhanced radio emission. In the first paper of this series, AGN detected with the International LOFAR Telescope (ILT) at 6'' were more likely to host an [O III] $\lambda 5007$ Å outflow than AGN not detected, although only high-powered jets were ruled out as the origin of radio emission. New wide-field, sub-arcsecond resolution imaging at 144 MHz with the ILT now enables a resolved morphological study of this sample. We present the first wide-field, sub-arcsecond images of the Boötes Deep Field at 144 MHz, detecting 4074 sources in the $\sim 0.3''$ image with a central sensitivity of $33.8 \mu\text{Jy beam}^{-1}$. For 47 AGN matched in AGN luminosity, we probe radio emission on kiloparsec-scales to investigate correlations with [O III] outflows. This sample spans $z < 0.83$, $10^{40} < L_{[\text{OIII}]} < 10^{43} \text{ erg s}^{-1}$, and $10^{21} < L_{144\text{MHz}} < 10^{24.5} \text{ W Hz}^{-1}$. We find that if we detect an AGN on both large-scales (6'') and small-scales (0.3''), 90 ± 7 per cent have an [O III] outflow, compared to 63 ± 9 per cent of sources detected on large-scales, but undetected on small-scales. Furthermore, 17 ± 6 per cent of sources without an [O III] outflow are detected on kiloparsec-scales, compared to 51 ± 12 per cent of sources with an [O III] outflow. This implies a connection between [O III] outflows and kiloparsec-scale radio emission, which is likely AGN-driven. In contrast, AGN without an [O III] outflow are dominated by diffuse radio emission, likely to be associated with star formation.

Key words: galaxies: active - quasars: emission lines - galaxies: kinematics and dynamics - techniques: interferometric - techniques: image processing - ISM: jets and outflows

1 INTRODUCTION

How feedback from Active Galactic Nuclei (AGN) operates is one of the major open questions in modern day astronomy. These accreting objects lie in the central regions of galaxies and are so powerful that they can alter the evolution of their host galaxy. This is clearly seen in both observations and simulations. Observations show that the mass of the Super Massive Black Hole (SMBH; Kormendy & Richstone 1992, 1995; Magorrian et al. 1998) is correlated with the velocity dispersion of their galaxy (Gebhardt et al. 2000; Merritt & Ferrarese 2001). Additionally, in cosmological simulations, AGN feedback is required to reproduce the observable Universe. For example, these

AGN provide crucial heating processes in these models (Bower et al. 2006; Croton et al. 2006). This feedback mechanism can be understood using a variety of observational techniques (see, Harrison & Almeida 2024, for a review). Although we can see the effects of AGN feedback occurring in our Universe, it still remains unclear how this feedback operates. One research area which can bring us closer to the answer is the study of AGN outflows.

AGN outflows can propagate into the interstellar medium (ISM) on kiloparsec scales and insert energy into the surroundings affecting a galaxies evolution (e.g., Fiore et al. 2017; Harrison et al. 2018; Veilleux et al. 2020). [O III] $\lambda 5007$ Å is a common tracer of ionised gas outflows and we can locate [O III] outflows by seeing if a second, broad, asymmetric, blueshifted, component is present. [O III] outflows have been linked to radio emission and investigating this

* E-mail: Emmy.Escott@csiro.au

connection helps us understand AGN feedback (e.g., [Rawlings et al. 1989](#); [Mullaney et al. 2013](#); [Nesvadba et al. 2017](#); [Zakamska et al. 2016](#); [Albán et al. 2024](#)). The narrow line region, where [O III] originates, typically spans a few kiloparsec, which is on a comparable scale to the radio emission we observe from steep spectrum radio cores (see, [Miley 1980](#), for a review), further demonstrating the link between [O III] and radio emission.

Previous works have begun to investigate the link between radio morphologies and [O III] emission, however these have been limited by the resolution of large radio surveys. [Molyneux et al. \(2019\)](#) obtained a sample of 2922 spectroscopically confirmed AGN below a redshift of 0.2, selected to be jet dominated. The authors used this sample to study the relationship between 1.4 GHz radio morphologies with [O III] kinematics. For their morphological classifications the authors utilised the radio survey Faint Images of the Radio Sky at Twenty-centimeters (FIRST; [Becker et al. 1995](#)) at an angular resolution of $\sim 5''$. Using a combination of machine learning and size measurements to classify radio morphology they found that compact sources have the most extreme [O III] gas kinematics. Another notable work connecting [O III] to radio emission is [Kukreti & Morganti \(2024\)](#). The authors build on the work of [Kukreti et al. \(2023\)](#) using the LOFAR Two-metre Sky Survey (LoTSS; [Shimwell et al. 2017, 2019, 2022](#)) alongside FIRST and the Very Large Array Sky Survey (VLASS; [Lacy et al. 2020](#)) to derive the spectral slopes for a sample of 5720 radio AGN and they study the [O III] line profiles using stacking analysis. They discover that peaked spectrum sources show more disturbed gas than non-peaked spectrum AGN, demonstrating that young jets have the strongest impact on [O III] kinematics. The authors extend this into a morphological study by defining compact radio emission where the FIRST deconvolved (DC) major axis size is $< 3''$ and extended radio emission where the DC major axis is $> 3''$. The authors find more distributed gas when a compact morphology is present compared to extended radio emission.

The studies above investigate radio emission at high frequencies with moderate angular resolution. In contrast, this paper is part of a series studying the connection between the properties of the [O III] $\lambda 5007 \text{ \AA}$ emission line and radio emission in a novel regime combining low-frequency with high angular resolution down to $0.3''$ allowing us to probe kpc-scale emission.

In our first paper, [Escott et al. \(2025\)](#) discovered that AGN detected in the LoTSS Deep Fields DR1 ([Sabater et al. 2021](#); [Tasse et al. 2021](#)) have a higher [O III] outflow detection rate (67.2 ± 3 per cent), compared to AGN without a detection (44.6 ± 3 per cent). This confirmed a clear link between low-frequency radio emission at 144 MHz and these ionised gas outflows as traced by [O III] $\lambda 5007$.

Using the standard $6''$ resolution, [Escott et al. \(2025\)](#) found that the majority of the radio detected AGN did not show a radio excess ([Delvecchio et al. 2017](#); [Best et al. 2023](#)) and therefore the origin of radio emission is not due to high-powered jets. We were unable to refine the origin of radio emission physically driving the increased [O III] outflow detection rate further because around 90 per cent of the radio detected sample were unresolved. Other possibilities for the emission could be low-powered jets (e.g. [Maini et al. 2016](#); [Jarvis et al. 2021](#); [Njeri et al. 2025](#)), shocks produced from wide angled disk winds which are AGN-driven (e.g. [Zakamska & Greene 2014](#); [Hwang et al. 2018](#); [Petley et al. 2022](#)), or star formation (e.g. [Vries et al. 2007](#); [Bonzini et al. 2015](#); [Padovani 2016](#); [Delvecchio et al. 2017](#)). Therefore, the question still remains: Which physical mechanism is driving the link between [O III] outflows and low-frequency radio emission?

Very long baseline interferometry (VLBI) allows us to produce high-resolution images which provides us with vital information on

the radio structures of sources. For example, the LeMMINGs survey conducted by e-MERLIN ([Baldi et al. 2018, 2020](#)) provides $\leq 0.2''$ resolution images of 280 nearby galaxies at 1.5 GHz while the Very Long Baseline Array (VLBA) can probe parsec-scale jet structures at 15 GHz such as in the MOJAVE survey (Monitoring of Jets in AGN with VLBA Experiments; [Lister & Homan 2005](#)). At similar frequencies as the VLBA the European VLBI Network (EVN) is capable of $\sim 0.025''$ (e.g. [Garrett et al. 2001](#); [Panessa & Giroletti 2013](#); [Kreuzinger et al. 2024](#)). Such high-resolution VLBI images give us invaluable information about the structures of radio sources to help entangle the origin of radio emission. While VLBI at high frequencies is relatively common practice, VLBI at low frequencies is particularly challenging due to the complex calibration strategies required to remove ionospheric directional dependent effects from visibilities.

The International LOFAR Telescope (ILT) is a powerful instrument to perform both wide area and deep high-resolution VLBI surveys ([Morabito et al. 2025a](#)). Three Deep Fields were released alongside LoTSS at standard $6''$ resolution: Lockman Hole, European Large Area Infrared Space Observatory Survey North 1 (ELAIS-N1), and Boötes ([Sabater et al. 2021](#); [Tasse et al. 2021](#)). ELAIS-N1 is now processed at its full depth of $10.7 \mu\text{Jy beam}^{-1}$ using 505 hours of observations and is, to date, the deepest low-frequency radio image produced ([Shimwell et al. 2025](#)). Creating sub-arcsecond images at 144 MHz is challenging due to ionospheric effects and hence, to date, only two wide-field images have been published at the highest resolution at 144 MHz. [Sweijen et al. \(2022\)](#) published a sub-arcsecond resolution image of the Lockman Hole using a 8-h integration time reaching a central sensitivity of $25 \mu\text{Jy beam}^{-1}$ with 2483 sources detected. A sub-arcsecond resolution image of ELAIS-N1 with an integration time of 32-hours is published in [de Jong et al. \(2024\)](#) with a depth of $14 \mu\text{Jy beam}^{-1}$ and 9203 source detections. This paper presents the first high-resolution images of the third Deep Field, Boötes. Therefore, we now have access to a combined area of $\sim 19 \text{ deg}^2$ of sub-arcsecond resolution images. A sub-arcsecond image of Euclid Deep Field North (EDFN; [Bondi et al. 2024](#)) will soon be available ([Bondi et al. in prep](#)) alongside a $\sim 2 \text{ deg}^2$ of Abell 2255 ([Rubeis et al. 2025, 2026](#)).

Now that we have access to three of the LoTSS Deep Fields at sub-arcsecond resolution, covering $\sim 19 \text{ deg}^2$, we can revisit the well-defined sample from [Escott et al. \(2025\)](#) which lies within the ILT's FoV to obtain their sub-arcsecond radio morphologies. In this paper, we use a combination of the low-frequency, sub-arcsecond morphology alongside brightness temperature measurements ([Morabito et al. 2022a, 2025b](#)) to identify the physical mechanism driving the low-frequency radio emission and its relation to the presence of [O III] outflows using our previous measurements from SDSS spectroscopy.

This paper is organised in the following sections: Section 2 describes the sample selection and the data including a summary of the [O III] fitting procedure from [Escott et al. \(2025\)](#). Section 3 describes the ILT data as well as presenting the first images of the Boötes field at sub-arcsecond resolution. Section 4 describes the morphological results. Section 5 discusses brightness temperature results. A discussion then follows in Section 6 and the conclusions are in Section 7. In this work we assume a WMAP9 cosmology ([Hinshaw et al. 2013](#)) with $H_0 = 69.32 \text{ km s}^{-1} \text{ Mpc}^{-1}$, $\Omega_m = 0.287$, and $\Omega_\Lambda = 0.713$.

2 SAMPLE SELECTION AND DEFINITIONS

Here, we briefly summarise the sample selection of the radio detected AGN from [Escott et al. \(2025\)](#). We take optical spectroscopic

measurements from SDSS using two catalogues: the SDSS DR16 Quasar catalogue (Lyke et al. 2020) and a broad line AGN catalogue (Liu et al. 2019). We locate sources which lie within the three Deep Fields from LoTSS Deep DR1 and remove AGN with $z > 0.83$ to ensure [O III] is visible in the SDSS spectra. We also remove spectra with a signal to noise (SNR) ratio below 5 and remove a further 31 AGN after visual inspection revealed poor quality spectra, (e.g., missing [O III] spectral information), leaving a sample of 198 AGN. We crossmatch these sources to the LoTSS Deep Fields DR1 using the catalogue of Kondapally et al. (2021). We find that 115 AGN have a detection in LoTSS, which in Escott et al. (2025) we coin the "radio detected AGN". In this paper we will only focus on the radio detected population as we are interested in linking the [O III] outflow detections to sub-arcsecond 144 MHz morphologies. To obtain these sub-arcsecond resolution images we use wide-field images produced using the ILT. The FoV for these images is smaller in comparison to the FoV of the Dutch stations due to the larger size of the international stations. Consequently, 50 radio detected AGN fall out of the international station FoV and the radio detected population decreases to 76. Therefore, for these 76 AGN we already have access to [O III] fitting results using SDSS, and do not need to conduct further spectroscopic decomposition.

2.1 [O III] Spectral Fitting and Outflow Diagnostics

We take the [O III] spectroscopic fits of the 76 ILT detected AGN as described in Escott et al. (2025). To summarise the fitting procedure, we use the fitting module, QUBESPEC¹ (Scholtz et al. 2021), which incorporates the Markov Chain Monte Carlo approach (MCMC; Goodman & Weare 2010). We fit various models to the spectra, for example one model will fit [O III] with a single Gaussian, and another will fit [O III] with two Gaussians. We also implement Fe-II templates in several of the models, for full details, see Escott et al. (2025). We firstly use the Bayesian Information Criterion (BIC) to select the model with the best fit to the data for each spectrum and confirm the selection via visual inspection.

In this paper, we are interested in whether the AGN hosts an [O III] outflow or not. We use the same three diagnostics to determine if an [O III] outflow is present as Escott et al. (2025). If two Gaussians produce the best fit to the emission line, we class this as an [O III] fitted outflow. When a single component has the best fit and the width of [O III] at 80 per cent of the flux (W_{80}) is over 800 km s^{-1} , we class this as an W_{80} outflow, and we class AGN as hosting a W_{80} likely outflow if one component is fitted and $600 \text{ km s}^{-1} < W_{80} < 800 \text{ km s}^{-1}$. This leaves AGN which have one Gaussian fitted with $W_{80} < 600 \text{ km s}^{-1}$ to be defined as not hosting an [O III] outflow.

We acknowledge that due to the complexity of the kinematics of [O III], the classifications above could lead us to missing outflowing structure in this emission line, for example AGN within our "no outflow" category could also show signs of outflows at smaller scales. For example, in Ward et al. (2024) the authors discuss that models demonstrate that physically slow outflows may not manifest themselves in optical spectroscopy. Therefore these weak outflows would be missed in our AGN within our "no outflow" population, meaning the [O III] outflows which we trace in this paper and Escott et al. (2025) are notably strong [O III] outflows.

To ensure that any morphological differences which appear between the outflowing and non-outflowing populations are not driven by a luminosity bias, we match the two populations in $L_{6\mu\text{m}}$ and

[O III] Outflow Type	Undetected	Compact	Extended	Total
[O III] Fitted Outflow	21 (13)	21 (12)	5 (4)	47 (29)
W_{80} Outflow	2 (1)	2 (1)	0 (0)	4 (2)
W_{80} Likely Outflow	4 (3)	2 (1)	0 (0)	6 (4)
All Outflows	27 (17)	25 (14)	5 (4)	57 (35)
No Outflow	14 (10)	5 (2)	0 (0)	19 (12)
Total	41 (27)	30 (16)	5 (4)	76 (47)

Table 1. Table summarising the number of AGN in each category of [O III] outflow and morphology type. The numbers in parentheses represent the $L_{6\mu\text{m}}$ and z matched population.

redshift, where $L_{6\mu\text{m}}$ is a tracer for AGN bolometric luminosity (Richards et al. 2006). We calculate this luminosity using the flux densities at $5.8\mu\text{m}$ and $8\mu\text{m}$ of the *Spitzer* Deep, Wide-Field Survey (SDWFS; Ashby et al. 2009) for AGN in Boötes, and *Spitzer* Wide-Area Infrared Extragalactic Survey (SWIRE; Lonsdale et al. 2003) fluxes for AGN in Lockman Hole or ELAIS-N1. We adopt the same tolerances used in Escott et al. (2025) of $\Delta z = 0.06$ and $\Delta \log L_{6\mu\text{m}} = 0.3$, as these successfully match our data as well as not substantially reducing our sample size. This reduces the overall AGN population from 76 AGN to 47, where we remove outliers in the $L_{6\mu\text{m}}$ and redshift distributions between the [O III] outflow and non-outflow populations, where 35 exhibit an [O III] outflow, while the remaining 12 show no evidence of such an [O III] outflow. We perform a 2D Kolmogorov-Smirnov (KS) test on these matched populations using the public code `ndtest`² and obtain a p-value of 0.192, confirming that the two populations are statistically indistinguishable. We present our matched $L_{6\mu\text{m}}$ and redshift population as coloured markers in the left subplot in Figure 1 and the unmatched AGN as grey markers, with AGN with [O III] outflows presented as stars, and AGN without an [O III] outflow as circles. The histograms represent the distribution in redshift (top) and $L_{6\mu\text{m}}$ (right), with the purple dashed histogram showing the outflowing population, and solid pink being the no outflow population. We show how many AGN are within each category and population in Table 1, including the morphological classes which we discuss in Section 4.

We present the relationship between $L_{144\text{MHz}}$ and $L_{[\text{OIII}]}$ on the right-hand side of Figure 1, with the $L_{6\mu\text{m}}$ and redshift matched population as coloured markers and circular markers as detected sources and downward triangles as the upper limit for the undetected sources. We calculate the k -corrected $L_{144\text{MHz}}$ for the detected AGN using the $0.3''$ flux density, the spectral index, α (where $S_\nu \propto \nu^{-\alpha}$), assuming a typical synchrotron spectral index of $\alpha = 0.7$ (Klein et al. 2018), and the SDSS spectroscopic redshift. To calculate the associated uncertainties, we use the reported scatter in the flux scaling correction in each field, 25 per cent for Boötes (see Section A2.1), 18 per cent for Lockman Hole, and 15 per cent for ELAIS-N1 and sum these uncertainties in quadrature with the flux density uncertainty from the source finding for each source. To calculate the upper limit of $L_{144\text{MHz}}$ for the undetected sources at $0.3''$, we take the relevant wide-field image and extract the 5σ noise level within a $3''$ radius of the source's location and use this as the associated flux density. We do not report uncertainties for the upper limits, as they are not direct measurements but rather thresholds defined at a specific confidence level. We utilise the $L_{[\text{OIII}]}$ presented in Escott et al. (2025) for these sources which are calculated by integrating the continuum-

¹ Available at <https://github.com/honzascholtz/Qubespec>

² Written by Zhaozhou Li, <https://github.com/syrte/ndtest>

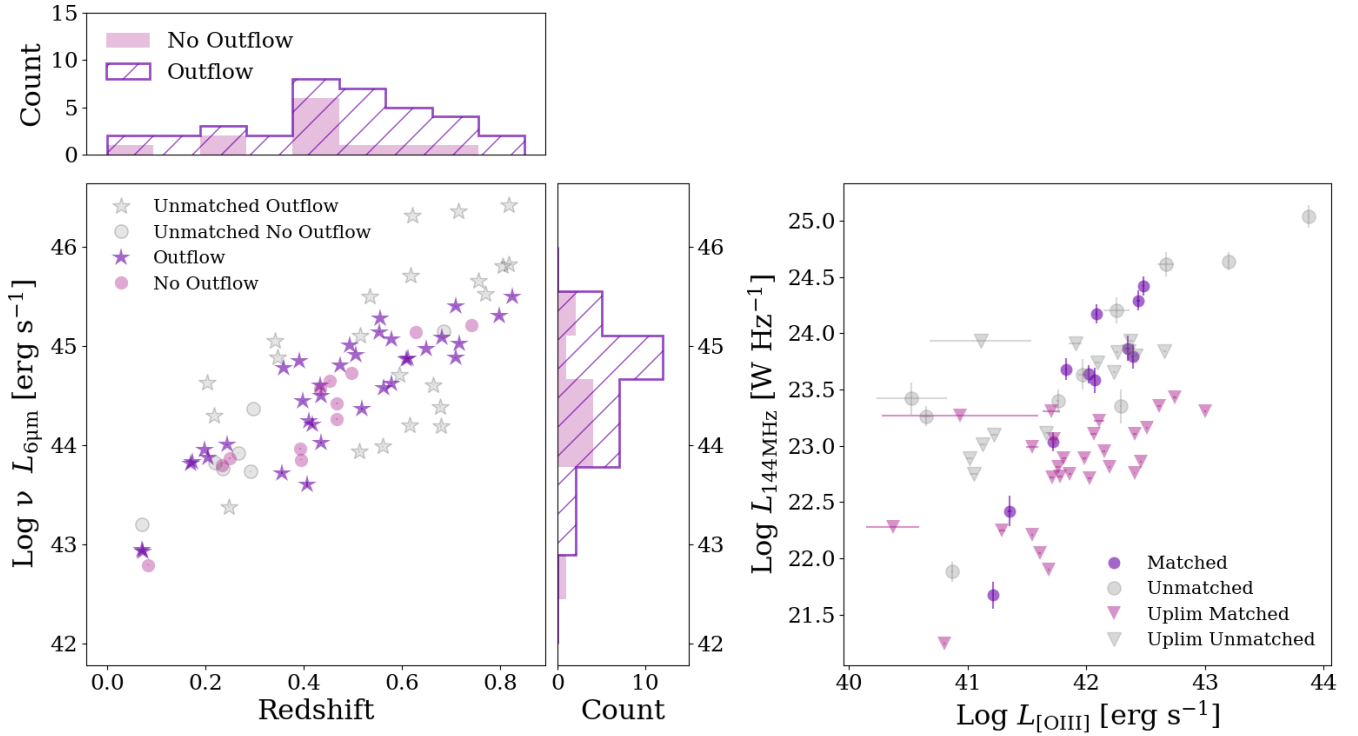


Figure 1. *Left:* The $L_{6\mu\text{m}}$ and redshift relation of the AGN with and without an [O III] outflow. The coloured markers show the matched populations in $L_{6\mu\text{m}}$ and redshift, with an [O III] outflow (purple stars) and without an [O III] outflow (pink circles). The grey points represent the AGN which are removed as these are unmatched, with diamonds portraying the AGN with [O III] outflows, and circles for the AGN without an [O III] outflow. We show uncertainties but these are minimal. The top histogram conveys the redshift distribution and the right histogram is the distribution of $L_{6\mu\text{m}}$. The hashed purple histograms are the AGN with [O III] outflows and the pink solid histograms are the AGN which do not have an [O III] outflow. *Right:* $L_{144\text{MHz}}$ as a function of $L_{[\text{OIII}]}$, the coloured markers are from the $L_{6\mu\text{m}}$ and redshift matched population we use in this analysis, and the grey are unmatched. $L_{144\text{MHz}}$ in this figure is calculated at $0.3''$. Circles represent the detected AGN and downward triangles are the upper radio luminosity limits.

subtracted region between 4975 \AA and 5030 \AA using spectroscopic redshifts and the distance modulus, and then this is converted to a luminosity. The inverse square root of the inverse variance is taken to compute the associated uncertainties and then the sum of the uncertainties is taken in quadrature. We see that our $L_{6\mu\text{m}}$ and redshift matched population follows a positive correlation between $L_{144\text{MHz}}$ and $L_{[\text{OIII}]}$, as expected.

3 DATA

3.1 LoTSS Deep Fields

For this investigation, we use the derived properties from LoTSS Deep Fields DR1 in Kondapally et al. (2021). Best et al. (2023) provides us with star formation rates for sources within the Deep Fields derived from Spectral Energy Distribution (SED) fitting.

We take the sub-arcsecond resolution morphologies and flux densities from the $0.3''$ resolution images at 144 MHz of Lockman Hole (Sweijen et al. 2022), ELAIS-N1 (de Jong et al. 2024), and Boötes. For our sample of AGN with $z < 0.83$, these sub-arcsecond resolution images allow us to probe low-frequency radio emission down to scales of $\sim 2 \text{ kpc}$, which now allows us probe down to sub-kiloparsec emission which is not possible at $6''$. Across all fields, these $0.3''$ resolution images contain $\sim 14,000$ sources at sub-arcsecond resolution.

Image	Resolution (arcsec ²)	Sensitivity ($\mu\text{Jy beam}^{-1}$)	Source Count
$0.3''$	$0.50'' \times 0.34''$	33.8	4074
$0.6''$	$0.67'' \times 0.60''$	44.2	4455
$1.2''$	$2.23'' \times 1.03''$	81.3	2480

Table 2. Summary of the three high-resolution Boötes images presented in this work: angular resolution of each image, sensitivity and source counts.

3.2 Boötes High-Resolution Images

Here, we release the first images of the Boötes Deep Field at $0.3''$, $0.6''$, and $1.2''$ at 144 MHz. The $0.6''$ and $1.2''$ images are important to understand the flux density distribution at different spatial scales. These high-resolution images and catalogues are available on the LOFAR surveys website³.

We present the $0.3''$ resolution image of the Boötes Deep Field in Figure 2. This image consists of 8.09 billion pixels, has a central sensitivity of $33.8 \mu\text{Jy beam}^{-1}$, a resolution of $0.50'' \times 0.34''$, contains 4074 sources with detections $\geq 5\sigma$ (where σ is the local RMS noise), and has an 8-h integration time.

Our $0.6''$ resolution image consists of 2.02 billion pixels with

³ The Boötes high-resolution images and associated catalogues are publicly available at: <https://lofar-surveys.org/hd-bootes.html>

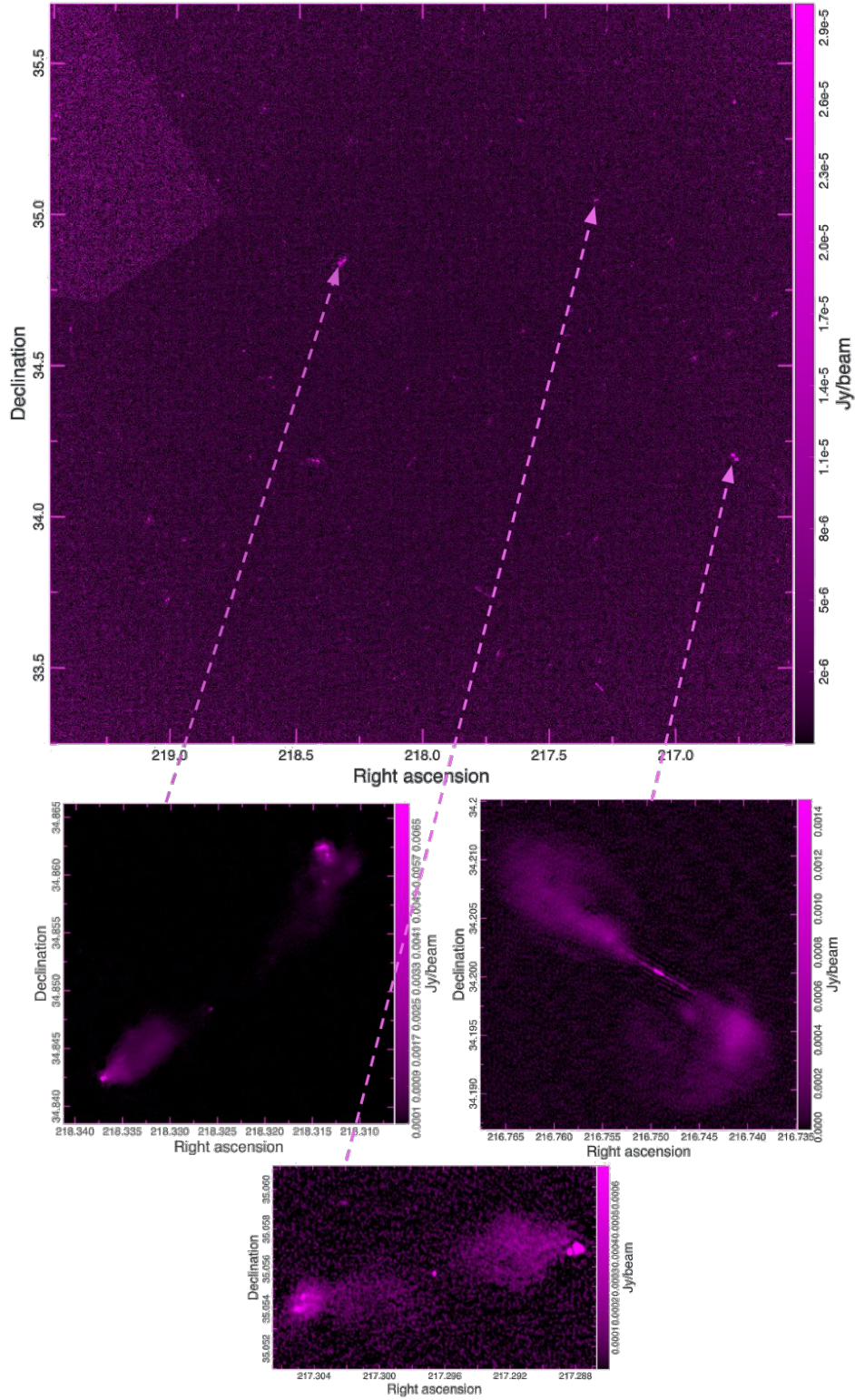


Figure 2. The first $\sim 0.3''$ resolution image of the Boötes Deep Field. This image consists of ~ 8 billion pixels, contains over 4,000 sources, and has a central sensitivity of $33.8 \mu\text{Jy beam}^{-1}$. The image is $2.5 \times 2.5 \text{ deg}^2$ with a restoring beam of $0.50'' \times 0.34''$. We highlight three interesting extended sources within this field beneath with the respective locations indicated by arrows. We can now probe radio emission of these sources to a new level thanks to the sub-arcsecond resolution.

4455 sources and has a central sensitivity of $44.2 \mu\text{Jy beam}^{-1}$ with a resolution of $0.67'' \times 0.60''$. At $1.2''$ the pixel number reduces to 0.506 billion with a source count of 2480 and a central sensitivity of $81.3 \mu\text{Jy beam}^{-1}$ with a resolution of $2.23'' \times 1.03''$.

3.3 High-resolution Wide-Field Imaging Considerations

This section briefly outlines the method we use to create the Boötes wide-field images using the ILT. For full details about the publicly available pipeline to produce VLBI images using the ILT, consult [Morabito et al. \(2022b\)](#) and for further information on the wide-field aspect of imaging using the ILT at sub-arcsecond, consult [Sweijen et al. \(2022\)](#) and [de Jong et al. \(2024\)](#). We summarise the details of the data reduction techniques we implement in Appendix A as it differs slightly from the above papers, due the fact that data processing pipelines were still in development at this time.

We retrieve the raw data of a 8-h observation to produce the high-resolution images of Boötes from the Long Term Archive (LTA⁴). The initial flux density calibrator observation has an observation ID of 726520 and the Boötes target field is 726524 with the project ID of LT10_10. The observation date is 2019-10-20 with a central position of right ascension (RA) 218.0° and declination (Dec) 34.5° . We use a frequency range of 121-166 MHz with 50 stations included in the final images: 24 core stations, 13 remote stations, and 13 international stations without the Swedish station (SE607), which we removed due to poor calibration solution for this station.

3.3.1 Systematic Effects

Radio data reduction relies heavily on calibration techniques that remove systematic effects embedded within the data visibilities. These systematic effects are removed by calibrating against a known in-field source, which we call a delay calibrator. An ideal calibrator source is a bright, compact, object which calibrates well through self-calibration cycles. Obtaining corrections using these calibrators allow us to understand how to calibrate for systematic effects across our FoV. We discuss in-field calibration in full using delay calibrators in Section A0.4.

There are two types of systematic effects present in the raw data. These are direction independent effects (DIEs) and direction dependent effects (DDEs). We briefly provide an overview of these effects; consult [de Gasperin et al. \(2019\)](#) for full details.

3.3.2 Direction Independent Effects

For ILT data reduction, the DIEs requiring correction are the polarisation offsets, the bandpass, and the clock offsets. LOFAR has two data streams, one for each of the X and Y polarisations. During observations these polarisations can deviate from each other, and therefore we must align the polarisations by applying a delay offset between the two streams. We calibrate these polarisations independently, allowing us to probe and correct for the offset between them. In this step, we assume that the calibrator sources are unpolarised. This polarisation offset is only present in the phases and is time independent. We therefore take one station as reference and apply a phase matrix which describes this delay offset causing the XX and YY streams to align.

Another DIE which we must correct for are systematic effects

present across the bandpass. When we take observations with interferometers such as the ILT, we measure visibilities, and these visibilities have non-physical units. By correcting for the bandpass, we convert these visibility units to the physical units of Janskys (Jy) as well as correcting for any variation in sensitivity across the frequency band. The bandpass affects both the XX and YY polarisation in the same way, however the corrections we require are different for each polarisation stream. These bandpass effects are time independent.

The final DIE we must correct for is the offset between different station clocks. Each remote and international station has its own independent clock (all core stations use the same clock) and over time these clocks drift from one another. When correcting for the clock offsets for the remote and international stations, we use the clock of the core stations as reference. All these clocks need to be synchronised to enable coherent signal processing across the vast network of stations which make up the ILT.

3.3.3 Direction Dependent Effects

The wide FoV of the ILT provides both advantages and challenges. The primary benefit is the increase in the number of sources that lie within one pointing and hence, in the wide-field mode of LOFAR-VLBI, we can produce wide-field images with thousands of sources within them. However, DDEs pose a significant challenge when reducing ILT data to sub-arcsecond resolution images. The DDEs are the ionospheric effects and the beam. These effects become more prominent at a wide-field scale, as ionospheric conditions exhibit variability on arc-minute scales, and can fluctuate across multiple degrees of the sky. It is therefore essential to correct for these effects when reducing ILT data.

The ILT's dipoles are fixed in place however, because the sources of interest move through the stations beam, any beam corrections we apply during calibration are time variable and the location of the source of interest within the FoV is directional dependent. When the dipole observations are correlated, the time and frequency of the observed phase varies between the stations and therefore this variation needs to be accounted for and thus a beam correction is applied.

The ionosphere poses the largest obstacle in LOFAR data reduction. The ionosphere is a layer of charged particles within the Earth's atmosphere. These particles interact with waves propagating through the atmosphere and as a result, these incoming waves become distorted in both phase and amplitude. These distortions have a frequency dependency of ν^{-2} , and hence have a larger effect at low-frequency ([Intema et al. 2009, 2011](#)). Therefore, in LOFAR observations, the ionosphere is the prevailing cause of DDEs. The effects are dependent on both the magnetic field strength along the line of sight and the Total Electron Content (TEC). The ionosphere poses a greater challenge for wide-field observations, as its conditions vary on degree scales. For VLBI, an even more serious concern is that ionospheric conditions can differ substantially between stations across Europe.

4 RADIO MORPHOLOGICAL CLASSIFICATION

To study the link between the presence of [O III] outflows and the high-resolution morphologies we must first place each of the 47 of our luminosity matched AGN within our sample into a morphology category. The image we use for this is at the highest resolution: $0.3''$. We define three categories: undetected, compact, and extended. AGN are classed as undetected if the source is not within the catalogues

⁴ <https://lta.lofar.eu/>

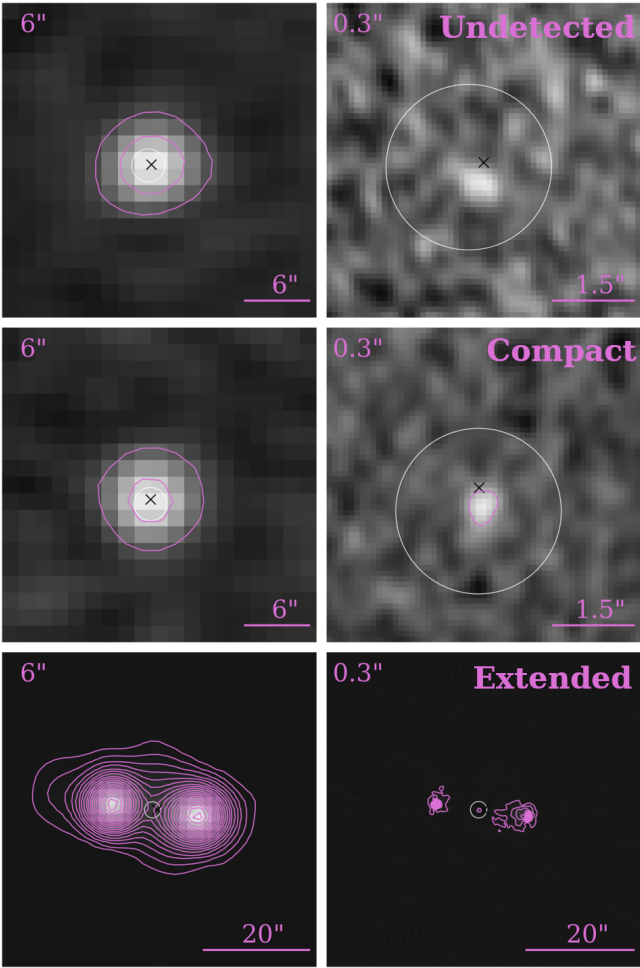


Figure 3. Demonstration of the morphology definitions in this work. *Left:* 6'' resolution, *right:* 0.3'' resolution. *Top:* Example of an "undetected" source, which does not have a 5σ detected at 0.3'' but is detected at 6''. *Middle:* A "compact" morphology. *Bottom:* "Extended" source. The black cross represents the LoTSS position, the white circle is the SDSS fibre and the contours are at a 5σ level.

published alongside the relevant field's image. We note that for these AGN which are undetected at 0.3'' resolution, the radio emission detected in the 6'' resolution image must be below the surface brightness sensitivity in the higher resolution image.

We define compact AGN in two ways. Images can suffer from ionospheric smearing, meaning an unresolved source maybe mistaken for an extended source via visual inspection. In an ideally calibrated image the ratio between the integrated flux density, S_I , and peak flux density, S_P , for an unresolved source will be equal to one. However, in reality this is not the case, but the natural logarithm of (S_I/S_P) follows a Gaussian distribution (Franzen et al. 2015) and we can utilise this alongside its standard deviation to determine whether a source is resolved. We follow the procedure performed in Shimwell et al. (2019, 2022) to determine if a source is unresolved. We first locate the best candidates for real point sources by finding sources classified as `S_code == 'S'` (pyBSDF has classified this source as a single compact component), and remove sources which are over three times (for Boötes and Lockman Hole) or four times (for ELAIS-N1) larger than the beam's major axis, as these sources could be resolved even if they are a single Gaussian component. For ELAIS-N1 we

use four times the major axis of the beam as this provides a better sigmoid fit because ELAIS-N1 uses four observation nights meaning this image suffers from greater ionospheric smearing than the other fields. Also two of the four ELAIS-N1 pointings are averaged to 2 seconds instead of 1, hence contributing to time smearing. We perform a sigmoid curve fit and if a source is below this fit, then the source is unresolved, and hence we classify the source as compact. If a source is above this divide then this is a resolved source and we perform visual inspection on these to classify their morphology as these sources may still be compact. If a source shows spatially resolved structure, we define this AGN as extended, and if the source shows visually compact morphology we define these as compact. To summarise, we class the sources which are determined to be unresolved using Shimwell et al. (2019, 2022) as compact and perform visual inspection on all other sources. We present three sources, one of each morphological class in Figure 3, where the left hand panels show the sources morphology at 6'' and on the right is the respective 0.3'' morphology.

We present an example source from the $L_{6\mu\text{m}}$ and redshift matched population which lies within the Boötes field in Figure 4. On the left we see the SDSS spectra for this AGN with the [O III] MCMC fit (from Escott et al. 2025) overlaid and from this fit we see that this AGN hosts an [O III] outflow, specifically a [O III] fitted outflow as a second, broad, blueshifted Gaussian is present. In the right panels of this figure, we present four cutouts of this source where we show purple 5σ contours. We start in the top left with the 6'' LoTSS cutout and proceeding clockwise with the 1.2'', 0.3'', and 0.6'' images. At all resolutions this source is extended.

4.1 Connecting Kiloparsec-Scale Radio Morphologies to Ionised Outflows

To help us understand whether there is a link between ionised outflows and physical processes which produce low-frequency radio emission, we first investigate the relationship between [O III] outflow detection rates and the sub-arcsecond resolution morphology of the AGN within our sample. In Figure 5 we present the link between the various [O III] outflow detection rates and morphology via two different methods. The detection rate of AGN with [O III] outflows is shown with purple stars and the detection rate for the population without an [O III] outflow is shown with pink circles. To estimate uncertainties, we assume a binomial distribution. Which is appropriate given the binary classification of sources as either outflowing or not. If the detection rate is equivalent to either 1 or 0, we do not show uncertainties. The grey dashed line separates the undetected AGN from the detected AGN. The results for Figure 5 are also shown quantitatively in Table 3.

On the left panel of Figure 5 we present the distribution of morphology class for sources with an [O III] outflow and those without an [O III] outflow, normalised by each [O III] outflow category i.e. for the AGN with [O III] outflows, summing the detection rates across the various morphological classes is equivalent to unity. We see that among AGN without [O III] outflows, the majority of these AGN, 83.3 ± 11 per cent, are undetected at sub-arcsecond resolution, compared to 48.6 ± 8 of the outflowing population showing an undetected morphology. This is consistent with the results in Escott et al. (2025). Sources with a compact morphology are more likely to host an [O III] outflow than not and all AGN which show extended radio structure at 0.3'' host an [O III] outflow.

The right panel of Figure 5 shows the fraction of the population with/without [O III] outflows per morphology category. Therefore, the sum of with and without [O III] outflows within each morphology

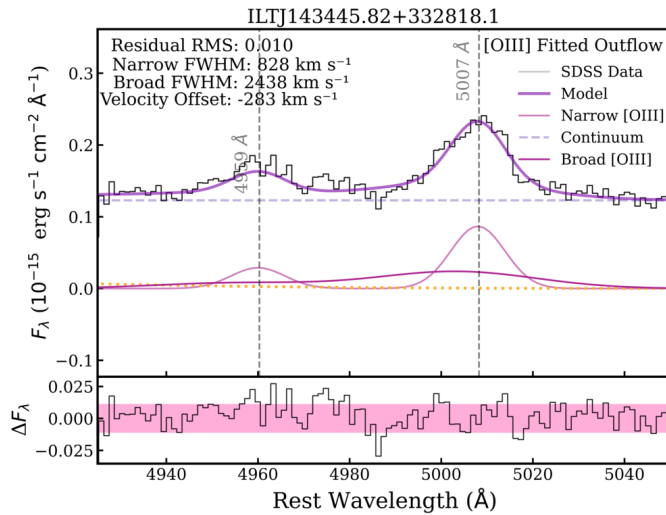
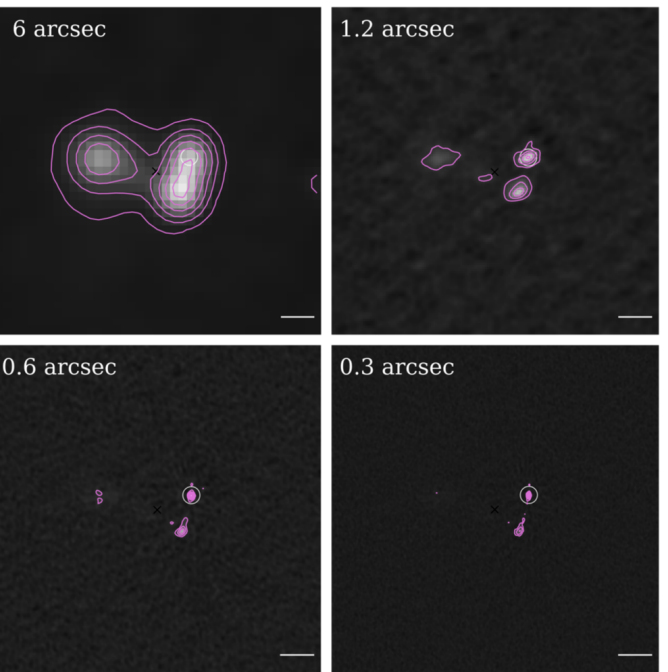


Figure 4. Montage showing the SDSS spectra and various morphologies of ILTJ143445.81+332818.1 ($z = 0.197$) which lie within the Boötes field. *Left:* SDSS spectra data (black) with the MCMC fitting results overlaid as a dark purple solid line. We display both the $\lambda 4959 \text{ \AA}$ and $\lambda 5007 \text{ \AA}$ [O III] emission lines. The pink Gaussians show the narrow component of [O III], the Gaussians in magenta are the broad component of [O III] which implies an [O III] outflow is occurring. The yellow dotted line shows the continuum. The lower panel of this subplot displays the residuals between the fitted model and SDSS data and the pink shaded region corresponds to the 1σ RMS region which we calculate over the full spectral range of the model. This AGN hosts an [O III] fitted outflow. *Right:* Cutouts of ILTJ143445.81+332818.1 at multiple resolutions. Starting top left and proceeding clockwise: $6''$, $1.2''$, $0.3''$, and $0.6''$ resolution. The background and the pink 5σ contours are from the respective resolution image. The scale bar in the bottom right corner demonstrates $6''$ and the white circle near the centre of each cutout is the location of the SDSS fibre. At each resolution this source has been classified as extended, and we believe the radio core is located in the northern components due to its compact structure.

category is equivalent to unity. We see that in all morphological categories, there are more AGN which host an [O III] outflow than to those which do not. This panel also reiterates that all four AGN with an extended structure host an [O III] outflowing structure, and hence there are no AGN without an [O III] outflow which have an extended morphology. In fact, even if we consider AGN which are not within our AGN luminosity and redshift matched population, all five extended sources have an [O III] outflow. We also note that, for our extended population, not all of the radio flux density is confined within the SDSS fibre, and therefore we could be missing an [O III] outflow from the spectroscopy. For example, see Figure 4, where the SDSS fibre only covers the the radio core of this extended source at $0.3''$ resolution. However every extended AGN is hosting an [O III] outflow so we are not missing [O III] outflows connected to the extended radio emission, but we could be missing additional [O III] emission associated with the radio emission which does not lie within the SDSS fibre.

To summarise, for AGN without [O III] outflows, most are undetected at $0.3''$, but are detected at $6''$. This indicates that the radio emission has low surface brightness which is not detectable at high-resolution. Synchrotron emission in star-forming galaxies arises from supernovae and their remnants. As the supernova rate is correlated to the star formation rate, synchrotron emission provides a tracer of recent star formation (Condon 1992). We assume that this synchrotron star formation is a widespread phenomena spread across the galaxy occurring on kpc scales (e.g. Walter et al. 2008; Tabatabaei et al. 2013; Heesen et al. 2019), so the radio emission associated with star



formation would be of a low surface brightness nature. It is consequently likely that if a source is detected at $6''$ but not $0.3''$ that the dominant radio emission mechanism is synchrotron star formation. If a galaxy has relatively intense star formation or is nearby, the low surface brightness emission could be above the detection limit and would manifest in a compact morphology. In such scenarios we can distinguish whether the radio emission is dominated by star formation or is AGN-driven using brightness temperature measurements (see Section 7). These assumptions are consistent with Morabito et al. (2022a).

In contrast, detected sources at high-resolution, are more likely to have [O III] outflows than not. To be detected at both large and small scales, these sources have high surface brightness. To produce such high surface brightness the source is likely to be dominated by AGN-driven processes such as wide angle disk winds or radio jets (e.g. Homan et al. 2006; Pötzel et al. 2021; Kravchenko et al. 2025). To distinguish the radio emission from winds and low-powered jets, simulations suggest we require milli-arcsecond resolution observations (Meenakshi et al. 2024). Therefore, we discuss wide-angle winds and low-powered jets together as AGN-driven phenomena. As discussed above, it is also possible that star formation can be above the detection limit and therefore we require brightness temperature measurements to determine whether the radio emission's origin is AGN-driven or due to star formation.

4.1.1 Estimating Physical Sizes

To investigate the structure of our sources at sub-arcsecond resolution, in Figure 6 we examine the relationship between the luminosity at 144 MHz, their physical size, and redshift indicated by the colour bar. For detected sources, we adopt the major axis as a proxy for physical size for sources within Lockman Hole and ELAIS-N1 as well as compact AGN within Boötes, but if a source is extended in Boötes we use the LAS (see Section A2.2). To estimate the lower limit angular sizes for the undetected sources, we extract the 5σ RMS noise from the $0.3''$ image for the relevant field, and using the flux density at $6''$, we calculate the major axis required for a source to be detected at $0.3''$, assuming a circular morphology. For the associated asymmetric uncertainties, we use the upper and lower bounds of the flux density and then proceed to calculate the major axis. We convert these angular sizes to physical sizes using WMAP9 cosmology and spectroscopic redshift from SDSS. We note for the undetected sources, the $L_{144\text{MHz}}$, and its uncertainties, are measured at $6''$ (presented in Escott et al. 2025), whereas for the detected sources, we use $0.3''$ measurements to calculate $L_{144\text{MHz}}$. The use of radio maps with different angular resolutions in calculating $L_{144\text{MHz}}$ may contribute to the apparent bimodality present between the detected and undetected sources.

In Figure 6, we depict compact sources with an [O III] outflow as crosses, compact sources without an [O III] outflow as circles, extended sources with a [O III] outflow as stars, and the undetected sources as triangles, with upward triangles indicating undetected sources with an [O III] outflow, and downward triangles as undetected sources without an [O III] outflow. The sizes of compact objects are upper limits, as they remain unresolved at sub-arcsecond resolution. We observe a positive correlation between the physical size of sources and the luminosity at 144 MHz in all populations, along with a general increase in redshift with both variables. The largest source in our detected population is an extended source in the Boötes field. The undetected sources follow a tight trend with redshift and radio luminosity because their sizes depend on both variables. This population exhibits larger physical sizes than the detected sources, with values between 4 kpc and 39 kpc.

5 BRIGHTNESS TEMPERATURE AS AN AGN DIAGNOSTIC

LOFAR, with its sub-arcsecond resolution at low frequencies and high sensitivity, offers surface brightness sensitivity comparable to VLBI observations at higher frequencies. This is therefore an ideal instrument to identify radio emission from AGN (Morabito et al. 2022a, 2025a). Star formation is expected to have a maximum surface brightness and anything above this must be produced by an AGN. Using the assumptions in Condon (1992), at an observed frequency of 144 MHz, the maximum value of brightness temperature produced by star formation is $\gtrsim 10^6$ K. Here we do not explicitly calculate brightness temperature for our sources, but rather the surface brightness.

Following Morabito et al. (2022a), we calculate the surface brightness using the total flux density and solid angle of the source, where the solid angle is,

$$\Omega = \frac{\pi\theta_1\theta_2}{4\ln 2}, \quad (1)$$

where θ_1 and θ_2 are the major and minor deconvolved axes. To determine the maximum surface brightness for star formation at

144 MHz, we use the same assumptions as Morabito et al. (2022a)⁵. We find that 9 of our 16 compact sources are inconsistent with star formation, and are therefore due to an AGN (56.25 per cent), with 7 (43.75 per cent) sources falling below the threshold for AGN activity. We note that the brightness temperature measurements are lower limits as these measurements are conducted on compact sources with upper size limits, therefore the 7 compact sources not classified as AGN at the current resolution could still have low-luminosity AGN cores, for example higher resolution VLBI data can reveal resolved, jet structures where sources are compact on kilo-parsec scales (e.g. Gabuzda et al. 1992; Giroletti et al. 2006; Kharb et al. 2021). Therefore, we cannot determine if these sources are consistent with star formation or AGN activity.

Figure 7 shows the relationship between Δ radio excess and log star formation rates (SFR), where the SFR are from Best et al. (2023), calculated by taking a consensus value from four different SED models. We only show detected sources at $0.3''$ in this Figure and we note one detected source within Boötes is not shown due to lack of SFR information. We flatten the radio excess and SFR- $L_{144\text{MHz}}$ relation to demonstrate the Δ radio excess as a function of SFR. We do this with respect to the Boötes radio excess definition as this field has a slight redshift adjustment (see Best et al. 2023, for more details; here we use the maximum redshift of our sample, $z=0.83$, in this redshift dependent relation) in comparison to the other two fields. We scale sources within Lockman Hole (blue) and ELAIS-N1 (yellow) to match the radio excess definition in Boötes (pink). We note that the $L_{144\text{MHz}}$ we use to obtain radio excess information is calculated using the $6''$ flux density as the SFR- $L_{144\text{MHz}}$ relation is derived using this resolution. Star markers show AGN with an [O III] outflow and circles show AGN without an [O III] outflow. Markers with a square around them are extended, and sources with a diamond are confirmed AGN from their T_b values.

Figure 7 shows us that 3 of the 4 extended sources are radio excess, demonstrating that the radio emission in these sources are AGN-driven. Combining this with the brightness temperature results, we see that the majority of sources detected at $0.3''$ are AGN dominated. We also note that all sources classified as an AGN via brightness temperature host an [O III] outflow, thereby compact sources with no [O III] outflow do not have an AGN identification.

6 DISCUSSION

6.1 ILT Wide-Field High-Resolution Image Comparison

Now that we have access to three sub-arcsecond Deep Field images, we will briefly discuss how the $0.3''$ image of Boötes compares to the other $0.3''$ images of Lockman Hole (Sweijen et al. 2022) and ELAIS-N1 (de Jong et al. 2024). The source count varies substantially between the three fields, with Lockman Hole having least (~ 2500), then Boötes (~ 4000), and ELAIS-N1 having the largest source count (~ 9000). The increased source count in ELAIS-N1 can clearly be explained because this image combines four different 8-h observations to create an image with a 32-h integration time. This results in the image being significantly deeper than both the Lockman Hole image and the Boötes image, which use single 8-h observations. The increased depth means that ELAIS-N1 probes

⁵ Electron temperature of 10^4 K, a synchrotron spectral index of -0.8 , and two key frequencies: the observed frequency of 144 MHz, as well as the assumed frequency of 3 GHz where synchrotron emission becomes optically thick.

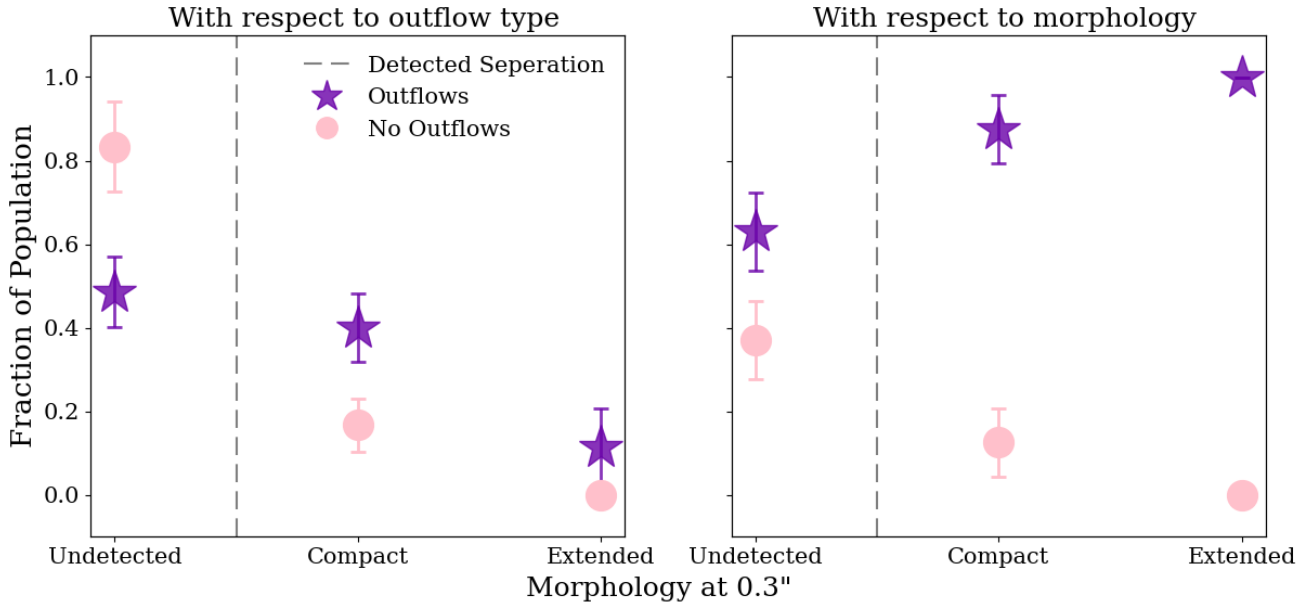


Figure 5. Fraction of population in relation to sub-arcsecond low-frequency radio morphologies, where a radio source is classified as either undetected, compact, or extended. *Left:* Distribution of morphology with respect to [O III] outflow population, i.e. for each [O III] outflow population, the fractions of different morphology categories add up to unity. *Right:* Distribution of [O III] outflow population with respect to the morphology category, i.e. for each morphology class, the fractions of the [O III] outflow population adds to unity. The pink circle markers demonstrate the no [O III] outflow population and the purple stars represent the outflowing population. In cases where the fraction of the population is either zero or one, the uncertainty is omitted. The grey dashed line separates the undetected AGN from the detected AGN.

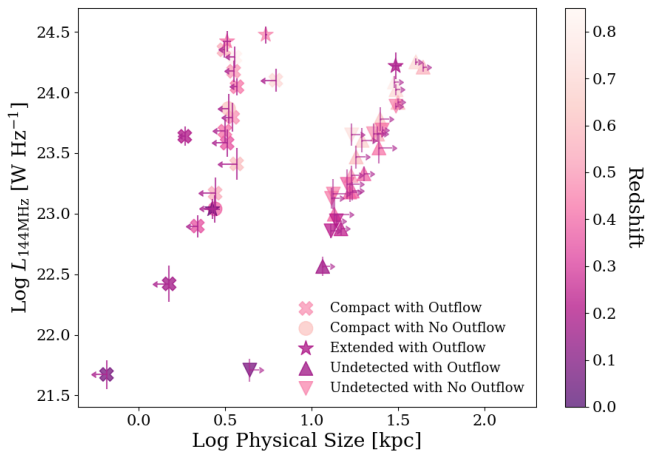


Figure 6. The relationship between the logarithm of the physical size, $\log L_{144\text{MHz}}$ and redshift (as traced by a colour bar). We show compact sources with an [O III] outflow as crosses, compact source without an [O III] outflow as circles, extended AGN with [O III] outflows as stars, undetected AGN with an [O III] outflow as upward-pointing triangles, and undetected AGN without an [O III] outflow as downward-pointing triangles. The sizes of compact sources are upper limits, while the sizes for undetected AGN are lower limits.

sources with lower flux densities than Boötes and Lockman Hole. The source count rapidly increases towards fainter radio luminosity and this hence explains the higher source count in this image (Shimwell et al. 2025).

The variation between source counts from Lockman Hole and Boötes can be understood in two ways. Firstly, significant progress

(a) with respect to outflow type

Morphology	Outflow	No Outflow
Undetected	48.6 ± 8	83.3 ± 11
Compact	40.0 ± 8	17.0 ± 6
Extended	11.4 ± 9	0 ± 0

(b) with respect to morphology

Population	Undetected	Compact	Extended
[O III] outflow	63.0 ± 9	87.5 ± 8	100 ± 0
No [O III] outflow	33.8 ± 9	12.5 ± 8	0 ± 0

Table 3. Tables summarising results shown in Figure 5 illustrating the connection between sub-arcsecond 144 MHz radio morphology and [O III] outflows. Table (a), with respect to [O III] outflow type. Table (b), with respect to morphology category. Values are percentages and we note that for Table (b), the uncertainties for the complementary categories are the same due to the binomial nature of the distribution.

has been made in the calibration strategies that we use to create these ILT wide-field images (see de Jong et al. 2024, for more detail). However this is unlikely to be the only reason for the increased source count. In this paper we use a different cataloguing strategy than the previous Deep Fields. For both Lockman Hole and ELAIS-N1 only sources that are also detected in the LoTSS Deep Field images which have an sub-arcsecond resolution counterpart associated are included in these field’s catalogues to ensure no false detections are present in them. For Boötes we take a different approach by keeping all sources detected by pyBDSF (which is on the order of 9000) and remove false detections by consulting the LoTSS noise map to see

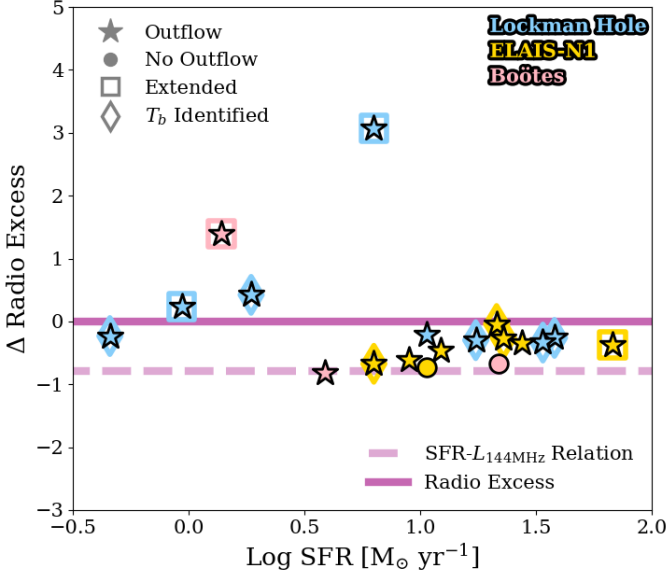


Figure 7. The relationship between Δ radio excess and log SFR. Only sources with a detection at $0.3''$ contribute to this figure. The pink solid line is the radio excess divide which is centred at $y = 0$, with the SFR and $L_{144\text{MHz}}$ relation as the dashed pink line. We define these relations using the Boötes field (pink), and hence we scale sources within Lockman Hole (blue) and ELAIS-N1 (yellow), which have a different radio excess definition, to match the Boötes definition. Star markers represent AGN with $[\text{O III}]$ outflows and circular markers show AGN without $[\text{O III}]$ outflows. Markers surrounded by a square have an extended morphology and sources with a diamond around them are confirmed AGN cores using brightness temperature measurements.

whether the high-resolution flux density recorded could be a noise fluctuation (see Section A2.2 for more detail). This also ensures we do not remove high-resolution components from sources, which are unresolved at $6''$ that have now become resolved at $0.3''$. Therefore by not removing these sources we ensure all real detections of extended sources are within the catalogues.

We further note that the $0.3''$, Boötes wide-field image has a higher noise level compared to the Lockman Hole image, despite both using a single 8-h observation. This is likely due to the low declination of the Boötes field because at low declinations calibration becomes more difficult.

6.2 Origin of Radio Emission from Radio-Quiet AGN

Although the radio-loud and radio excess classes are defined in different ways, they both seek to identify where the radio emission is clearly dominated by AGN. The converse to these populations is considered to be ‘radio-quiet’ AGN and it is unclear what is the dominant form of radio emission in these sources (e.g. Laor & Behar 2008; Panessa et al. 2019; Baldi et al. 2021).

Figure 7 shows the relationship between SFR and radio luminosity at 144 MHz. A similar figure is also shown in Escott et al. (2025), however in this paper we add morphological information alongside brightness temperature identifications. We continue to see the majority of sources to be non-radio excess when a $0.3''$ detection is present. Only four sources lie above the radio excess divide (ILTJ143445.82+332818.1, ILTJ104058.81+581703.4, ILTJ105141.05+591305.4, and ILTJ105421.20+572544.2), and all the AGN showing radio excess host an $[\text{O III}]$ outflow. This tells us

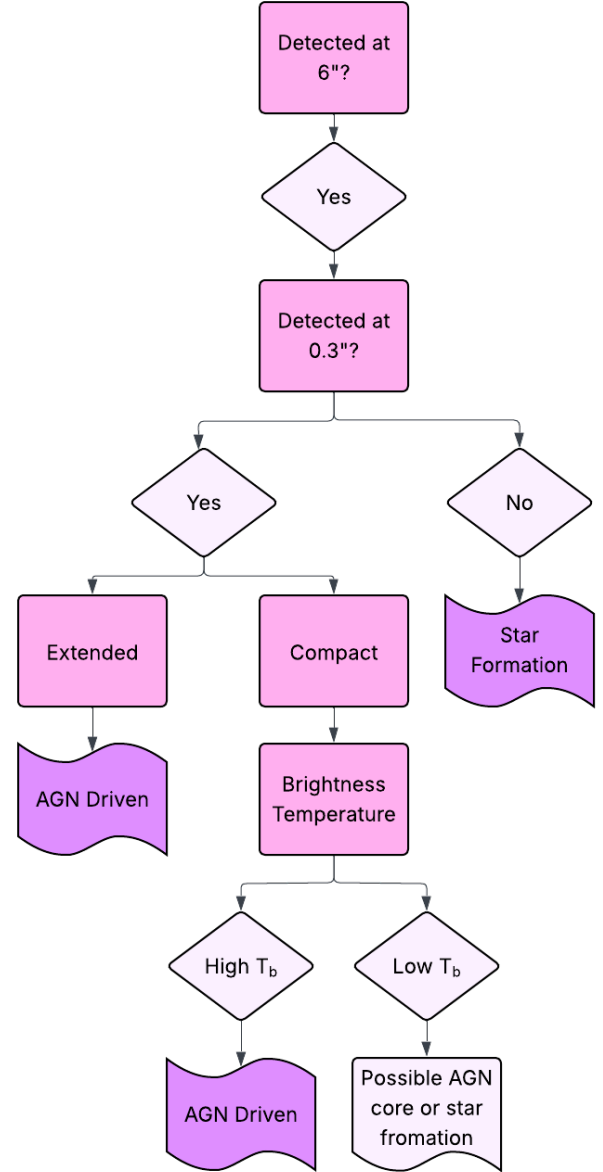


Figure 8. A decision tree demonstrating the procedure we use to determine the origin of radio emission from an AGN.

that the radio mechanism produced by these radio AGN can not be produced by star formation alone and is likely to be produced by radio jets. Thus the origin of radio emission from 3 of the 4 extended sources is AGN-driven due to their radio excess nature. We would also assume that the radio emission from extended sources at high-resolution is AGN-driven as we can visibly see a radio jet in these sources such as in Figure 4. The other radio excess source is compact as well as being a radio AGN core, as confirmed using brightness temperature (ILTJ105421.20+572544.2). As this is a radio AGN core, there will be a radio jet present (e.g. Blandford & Königl 1979) which at this resolution with this frequency is unresolved. So we can now confirm that for the radio excess AGN, the radio emission is produced by radio jets and therefore the dominant radio mechanism is AGN-driven.

For AGN which are not radio excess, we could previously only rule out that the dominant radio emission mechanism was high powered jets. Due to the new high-resolution images, we can now look at the morphologies and brightness temperatures of the sources to determine the dominant radio emission mechanism. In the non-radio excess sources, we see a mix of sub-arcsecond morphologies, containing AGN with compact morphologies, some being a confirmed radio AGN core and some not, and also a single extended AGN. We also note that all AGN which do not host an [O III] outflow are non-radio excess, show a compact morphology, and are not a detected radio AGN core.

It is also important to highlight that for our 42 radio-quiet AGN, 64.3 ± 7 per cent are detected at $6''$ and are undetected at $0.3''$. As previously discussed, the responsible mechanism of this emission would likely be due to the large scale phenomenon of star formation. Therefore, the radio emission is not due to jet and/or hotspots or AGN core emission. For clarity, we present a decision tree in Figure 8 which demonstrates the procedure in which we determine the origin of radio emission depending on both morphologies and brightness temperature.

We note that for sources detected at $6''$ but not at $0.3''$, the radio emission could originate from remnant emission associated with previous AGN activity rather than star formation. However, [Jurlin et al. \(2021\)](#) shows that only 7 per cent of a sample of active, restarted and remnant candidates identified by [Brienza et al. \(2017\)](#) are confirmed remnant radio sources. Given the expected scarcity of these sources, we therefore classify the sources undetected at $0.3''$ as star-forming. To confirm whether the radio emission arises from remnant AGN activity rather than star formation requires spectral index measurements. If a significant fraction of these sources are dominated by remnant AGN emission, this would imply a long remnant phase and a correspondingly low AGN duty cycle, given the high fraction of sources undetected at $0.3''$.

Summing all this up, in this population of 42 non-radio excess AGN, i.e. radio-quiet AGN, there appears to be a combination of mechanisms driving the radio emission. Star formation appears to drive 64.3 ± 7 per cent (27 out of 42) of these AGN, as the majority of sources are not detected at small scales ($0.3''$). Small scale AGN-driven emission is also driving a considerable amount of the radio emission as 19.0 ± 6 per cent (8 out of 42) show either an extended morphology, indicating small scale jets, or are a high T_b core.

6.3 Driving Radio Mechanism of [O III] outflows

We discuss how Figure 5 provides us with insight about the relationship between sub-arcsecond resolution morphology and the detection rates in the [O III] outflow and no [O III] outflow populations. We see that the majority of AGN without an [O III] outflow are undetected at $0.3''$, but detected at $6''$. Therefore, the emission from undetected AGN is produced on large scales, as demonstrated in Figure 6, and hence is consistent with star formation. We show the physical size distribution of our detected sources in Figure 9 (see Section 4.1.1 for details about size calculation). The physical sizes are all under 7 kpc, aside from one extended source which is >30 kpc. Hence, emission on the scale of $0.3''$ is small-scale.

Around half of the AGN with [O III] outflows are undetected at $0.3''$, also indicating that this emission is driven by star formation. The remaining half of AGN with [O III] outflows are detected at $0.3''$, with all extended AGN and all high T_b cores hosting an [O III] outflow. This implies that the radio emission is consistent with AGN-driven activities.

The differences we see between the outflowing population and non-

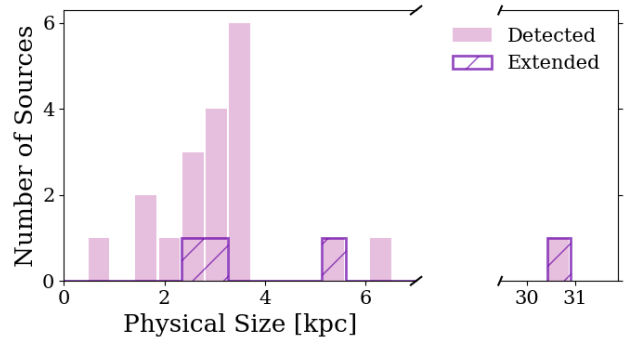


Figure 9. Histogram showing the distribution of the physical sizes in kpc of the detected sources at $0.3''$. The pink solid histogram shows all detected AGN within the $L_{6\mu\text{m}}$ and z matched population. The purple dashed histogram shows the sizes of the extended AGN. The figure includes a break in the x-axis to account for a single outlying source with a physical size of approximately 30.5 kpc.

outflowing population is not driven by an AGN luminosity bias as we have matched in $L_{6\mu\text{m}}$ and z and we note that the radio luminosity at $0.3''$ for the extended sources, is not significantly higher than the radio luminosity for the compact sources ($<2\sigma$).

[O III] traces recent nuclear activity as it is produced from a region about 1 kpc in size, however the radio emission produced by extended radio structure which can stretch 100s of kpc occur on a much longer time scale of 10^8 years. Therefore if the central engine has recently been shut down, the narrow line region, and hence [O III], may no longer be detected in the AGN, although the radio lobes will still be present. Therefore, for our detected sources, where we are mostly probing emission on scales <10 kpc, the timescales of nuclear activity traced by [O III] are likely comparable to those of the associated radio emission. In contrast, for our undetected sources the emission is on larger scales, which is unlikely to be physically associated with the same timescales as the nuclear [O III] activity.

Putting all this together, we are seeing a physical link between small scale radio emission due to AGN activity, and ionised gas outflows, as traced by [O III]. The majority of sources which do not host an [O III] outflow are undetected at $0.3''$, whereas the majority of sources with a compact morphology host an [O III] outflow. Furthermore, all the sources with a compact morphology that are also a T_b core AGN, host an [O III] outflow and all spatially resolved sources host an [O III] outflow. This supports the idea that small scale emission produced by the AGN core, radio jets, disk winds, and/or hotspots plays a key role in driving these [O III] outflows, while more diffuse, large scale emission from star formation is not a main driver. However, it appears overall that for AGN with [O III] outflows there is around equal amounts of small and large scale emission contributing to the driving mechanism of these [O III] outflows as $\sim 49 \pm 8$ per cent of AGN with [O III] outflows are undetected in the $0.3''$ image.

In Appendix B we investigate how [O III] kinematics vary between the detected AGN population and the undetected population. This is similar analysis to [Escott et al. \(2025\)](#), although the authors investigate the radio emission at $6''$, whereas here we are probing emission at $0.3''$. We see similar enhanced integrated flux of the broad area as well as enhanced W_{80} in the detected AGN compared to the undetected AGN. This suggests the enhancement we see is not driven by the radio emission which is resolved out between $6''$ and $0.3''$. Due

to the limited sample size and lack of uncertainties we do not draw conclusions from Figures B1 and B2.

6.4 Comparing Kpc-Scale Radio Emission and [O III] Studies

When investigating the origin of radio emission it is important to compare the results we see in this work to other work conducted at other frequencies and resolutions. Jarvis et al. (2019) follows up 10 low redshift radio quiet AGN which are originally selected in Mullaney et al. (2013) with images from the VLA and e-MERLIN. VLA images are between 0.3 and 1 arcseconds with a frequency range of 1.5-6 GHz and e-MERLIN images having a resolution around $0.25''$ at 1.5 GHz for 9 targets and they discover that star formation only accounts for ~ 10 per cent of the radio emission with around 90 per cent of these 9 targets showing extended radio structures on 1-25 kpc scales.

Njeri et al. (2025) presents similar work but at higher resolution with 42 e-MERLIN images at 6 GHz of low redshift quasars from the Quasar Feedback Survey. These images allow the authors to investigate sub-kiloparsec emission. Similarly to this study the authors use a combination of morphology and brightness temperature to classify their AGN. Combining these e-MERLIN and previous VLA images from Jarvis et al. (2021) they find that over 86 per cent of these quasars are classified as radio AGN and therefore this emission is likely to be dominated by jet driven lobes and outflow driven shocks.

The results from Jarvis et al. (2019, 2021) and Njeri et al. (2025) appear to be contradictory to the results we present in this work, as we see that the majority of our matched AGN (27 out of 47) are undetected at 144 MHz and $0.3''$ resolution and therefore the majority of the radio emission appears to be from star formation. A key reason for the difference could be due to the low redshift nature of the samples presented in these as the AGN from these studies are below 0.2 redshift, whereas our sample spans to around 0.85. We note that the four extended sources within our sample are at low redshift. The high angular resolution images from the VLA and e-MERLIN in Jarvis et al. (2019, 2021) are at GHz frequencies whereas the high-resolution images for our sample are at MHz frequencies so we are probing a different regime of emission where the radio emission from the *ILT* is dominated by synchrotron emission. At GHz frequencies, there is an increased contribution from Bremsstrahlung emission. We also note that the selection of their targets is based on strong [O III] emission whereas our sample is optically selected and independent of [O III] properties until we split the population into sources with an [O III] outflow and those without. We see a clear correlation with [O III] outflows in our sample and resolved emission, therefore it may be the presence of powerful [O III] emissions that could be driving the kpc-scale and sub-kpc-scale resolved emission that is seen in Jarvis et al. (2019, 2021) and Njeri et al. (2025). Finally, the Quasar Feedback Survey targets AGN with AGN luminosity above 10^{45} erg s^{-1} , whereas all our AGN have an AGN luminosity below 10^{45} erg s^{-1} . The radio luminosities of sources in this survey is higher than ours. Taking a spectral index of -0.7 our sample probes emission down to $L_{1.4\text{GHz}} \sim 10^{20}$ W Hz^{-1} . Therefore, these studies and ours lie in a different regime of both radio and AGN luminosity.

This high-resolution resolved study of the connection between [O III] and radio emission is consistent with previous unresolved analysis, which attribute the link to AGN activity (e.g., Molyneux et al. 2019; Kukreti et al. 2025). In addition, resolved Integral Field Unit (IFU) studies of individual sources, or small samples, have demonstrated that radio jets strongly interact with the ISM (e.g., Venturi et al. 2021; Girdhar et al. 2022; Speranza et al. 2024), in agreement with predictions from simulations (Meenakshi et al. 2022).

IFU follow-up for the resolved, extended sources in our sample will therefore help us to disentangle the spatial interplay between ionised outflows and the ISM.

7 CONCLUSIONS

We present sub-arcsecond, kpc-scale morphological results for 47 optically selected AGN from Escott et al. (2025), matched in $L_{6\mu\text{m}}$ and redshift, which lie within the *ILT* FoV of the LoTSS Deep Fields. Using wide-field VLBI techniques, we additionally release the first high-resolution images of the Boötes Deep Field at 144 MHz, presented at $\sim 0.3''$, $\sim 0.6''$, and $\sim 1.2''$. The $\sim 0.3''$ image achieves a sensitivity of $33.8 \mu\text{Jy beam}^{-1}$ with $4074 5\sigma$ source detections.

For the 47 sources for which we have both [O III] information and kpc-scale radio images, we define three morphological categories: undetected AGN, where these sources are detected at $6''$ but are undetected at $0.3''$, compact AGN, which are unresolved at this resolution, and extended AGN, which show spatially resolved emission. We further separate our sample into two populations: AGN which host an [O III] outflow (35 AGN), and another where the AGN do not host an [O III] outflow (12 AGN). Below we present the key findings in this work:

- Outflows traced by [O III] appear to be AGN-driven for the following reasons:
 - If AGN are detected at both small, kpc-scales ($0.3''$) and large-scales ($6''$), 90 ± 7 per cent host an [O III] outflow.
 - All 9 detected compact sources which are a high T_b radio core host an [O III] outflow.
 - All four detected, extended sources host an [O III] outflow
 - 87.5 ± 8 per cent of sources with a compact morphology host an [O III] outflow.
- AGN without an [O III] outflow are likely dominated by synchrotron star formation because:
 - 83.3 ± 11 per cent of sources without an [O III] outflow are undetected on kpc-scales.
- The origin of radio emission from the radio-quiet AGN is dominated by star formation as:
 - 64.3 ± 7 per cent of the non-radio excess AGN are undetected on small-scales.
 - A considerable amount of the radio emission does appear to be AGN-driven as 19.0 ± 6 per cent of the radio-quiet population are either extended or are a high T_b AGN core.

We acknowledge that our sample size is limited, with 35 AGN with [O III] outflows and 12 without, primarily due to the limited number of sources with SDSS spectroscopy within the *ILT* coverage of the LoTSS Deep Fields. The upcoming deep tier of the WEAVE-LOFAR survey (Smith et al. 2016) is expected to produce an estimated 130,000 spectroscopic measurements of bright sources in these fields, many with sub-arcsecond morphologies. Furthermore, the first data release from the Dark Energy Spectroscopic Instrument (DESI; DESI Collaboration et al. 2025) will also increase spectroscopic coverage. Together with the intermediate resolution images of Boötes and ELAIS-N1 (de Jong et al. 2024; Ye et al. 2024) at $\sim 0.6''$ and $\sim 1.2''$, we can extend our high-resolution studies to investigate emission too diffuse to detect at the highest resolution.

ACKNOWLEDGEMENTS

We thank Daniel Smith for his useful insights on this paper. ELE and LKM are grateful for support from the Medical Research Council [MR/T042842/1]. FS and LKM appreciate the support of STFC [ST/Y004159/1]. JMGHJdJ acknowledges support from project CORTEX (NWA.1160.18.316) of research programme NWA-ORC, which is (partly) financed by the Dutch Research Council (NWO). JMGHJdJ and RvW acknowledge support from the OSCARS project, which has received funding from the European Commission's Horizon Europe Research and Innovation programme under grant agreement No. 101129751. CMH acknowledges funding from an United Kingdom Research and Innovation grant (code: MR/V022830/1). IP acknowledges support from INAF under the Large Grant 2022 funding scheme (project "MeerKAT and LOFAR Team up: a Unique Radio Window on Galaxy/AGN co-Evolution").

This paper is based on data obtained with the International LOFAR Telescope (ILT). LOFAR (Haarlem et al. 2013) is the low-frequency Array designed and constructed by ASTRON. It has observing, data processing, and data storage facilities in several countries, that are owned by various parties (each with their own funding sources), and that are collectively operated by the ILT foundation under a joint scientific policy. The ILT resources have benefited from the following recent major funding sources: CNRS-INSU, Observatoire de Paris and Université d'Orléans, France; BMBF, MIWF-NRW, MPG, Germany; Science Foundation Ireland (SFI), Department of Business, Enterprise and Innovation (DBEI), Ireland; NWO, The Netherlands; The Science and Technology Facilities Council, UK; Ministry of Science and Higher Education, Poland; The Istituto Nazionale di Astrofisica (INAF), Italy.

This research made use of the Dutch national e-infrastructure with support of the SURF Cooperative (e-infra 180169) and the LOFAR e-infra group. The Jülich LOFAR Long Term Archive and the German LOFAR network are both coordinated and operated by the Jülich Supercomputing Centre (JSC), and computing resources on the supercomputer JUWELS at JSC were provided by the Gauss Centre for Supercomputing e.V. (grant CHTB00) through the John von Neumann Institute for Computing (NIC).

This work used the DiRAC at Durham facility managed by the Institute for Computational Cosmology on behalf of the STFC DiRAC HPC Facility (www.dirac.ac.uk). The equipment was funded by BEIS capital funding via STFC capital grants ST/P002293/1, ST/R002371/1 and ST/S002502/1, Durham University and STFC operations grant ST/R000832/1. DiRAC is part of the National e-Infrastructure.

This work has been enabled by access to facilities and the scientific and technical support provided by the UK SKA Regional Centre (UKSRC). The UKSRC is a collaboration between the University of Cambridge, University of Edinburgh, Durham University, University of Hertfordshire, University of Manchester, University College London, and the UKRI STFC Scientific Computing (STFC) at RAL. The UKSRC is supported by funding from the UKRI STFC.

This work has made use of the University of Hertfordshire's high-performance computing facility. This work also made use of SciPy, NumPy, Matplotlib and Astropy.

DATA AVAILABILITY

The complete catalogue of the 198 AGN presented in Escott et al. (2025), including the 76 AGN detected in the ILT which we discuss in this paper, will be available on CDS on publication. This catalogue includes the [O III] fitting properties.

The Boötes high-resolution images and associated catalogues will be publicly available at the time of publication at: <https://lofar-surveys.org/hd-bootes.html>. The Lockman Hole high-resolution image and associated catalogue are publicly available at: <https://lofar-surveys.org/hdfields.html>. The ELAIS-N1 high-resolution images and catalogues are publicly available at: <https://lofar-surveys.org/hd-en1.html>.

We use the SDSS Quasar catalogue from DR16 which can be accessed at https://www.sdss4.org/dr17/algorithms/qso_catalog/ and the broad-line AGN catalogue from SDSS DR7 which can be found at <https://cdsarc.u-strasbg.fr/cgi-bin/ftp-index?ftp/cats/J/ApJS/243/21>. The SDSS spectra used in the spectral fitting can be downloaded from <https://skyserver.sdss.org/dr19/SearchTools/SQS> by uploading the source's location or plate information.

REFERENCES

- Albán M., Wylezalek D., Comerford J. M., Greene J. E., Riffel R. A., 2024, *Astronomy & Astrophysics*, 691, A124
- Ashby M. L. N., et al., 2009, *The Astrophysical Journal*, 701, 428
- Baldi R. D., et al., 2018, *Monthly Notices of the Royal Astronomical Society*, 476, 3478
- Baldi R. D., et al., 2020, *Monthly Notices of the Royal Astronomical Society*, 500, 4749
- Baldi R. D., Laor A., Behar E., Horesh A., Panessa F., McHardy I., Kimball A., 2021, *Monthly Notices of the Royal Astronomical Society*, 510, 1043
- Becker R. H., White R. L., Helfand D. J., 1995, *The Astrophysical Journal*, 450, 559
- Bertin E., Mellier Y., Radovich M., Missonnier G., Didelon P., Morin B., 2002, p. 228, <https://ui.adsabs.harvard.edu/abs/2002ASPC..281..228B>
- Best P. N., et al., 2023, *Monthly Notices of the Royal Astronomical Society*, 523, 1729
- Blandford R. D., Königl A., 1979, *The Astrophysical Journal*, 232, 34
- Bondi M., et al., 2024, *Astronomy & Astrophysics*, 683, A179
- Bonzini M., et al., 2015, *Monthly Notices of the Royal Astronomical Society*, 453, 1079
- Bower R. G., Benson A. J., Malbon R., Helly J. C., Frenk C. S., Baugh C. M., Cole S., Lacey C. G., 2006, *Monthly Notices of the Royal Astronomical Society*, 370, 645
- Brienza M., et al., 2017, *Astronomy & Astrophysics*, 606, A98
- Charlot P., et al., 2020, *Astronomy & Astrophysics*, 644, A159
- Condon J. J., 1992, *Annual Review of Astronomy and Astrophysics*, 30, 575
- Croton D. J., et al., 2006, *Monthly Notices of the Royal Astronomical Society*, 367, 864
- DESI Collaboration D., et al., 2025, Data Release 1 of the Dark Energy Spectroscopic Instrument, doi:10.48550/arXiv.2503.14745, <http://arxiv.org/abs/2503.14745>
- Delvecchio I., et al., 2017, *Astronomy & Astrophysics*, 602, A3
- Escott E. L., et al., 2025, *Monthly Notices of the Royal Astronomical Society*, 536, 1166
- Fiore F., et al., 2017, *Astronomy & Astrophysics*, 601, A143
- Franzen T. M. O., et al., 2015, *Monthly Notices of the Royal Astronomical Society*, 453, 4020
- Gabuzda D. C., Cawthorne T. V., Roberts D. H., Wardle J. F. C., 1992, *The Astrophysical Journal*, 388, 40
- Garrett M. A., et al., 2001, *Astronomy & Astrophysics*, 366, L5
- Gebhardt K., et al., 2000, *The Astrophysical Journal*, 539, L13
- Girdhar A., et al., 2022, *Monthly Notices of the Royal Astronomical Society*, 512, 1608
- Giroletti M., Giovannini G., Taylor G. B., 2006, *Proceedings of the 8th European VLBI Network Symposium*, p. 22
- Goodman J., Weare J., 2010, *Communications in Applied Mathematics and Computational Science*, 5, 65

- Haarlem M. P. v., et al., 2013, *Astronomy & Astrophysics*, 556, A2
- Harrison C. M., Almeida C. R., 2024, Observational Tests of Active Galactic Nuclei Feedback: An Overview of Approaches and Interpretation, doi:10.48550/arXiv.2404.08050, <http://arxiv.org/abs/2404.08050>
- Harrison C. M., Costa T., Tadhunter C. N., Flütsch A., Kakkad D., Perna M., Vietri G., 2018, *Nature Astronomy*, 2, 198
- Heesen V., et al., 2019, *Astronomy & Astrophysics*, 622, A8
- Hinshaw G., et al., 2013, *The Astrophysical Journal Supplement Series*, 208, 19
- Homan D. C., et al., 2006, *The Astrophysical Journal*, 642, L115
- Hwang H.-C., Zakamska N. L., Alexandroff R. M., Hamann F., Greene J. E., Perrotta S., Richards G. T., 2018, *Monthly Notices of the Royal Astronomical Society*, 477, 830
- Intema H. T., Tol S. v. d., Cotton W. D., Cohen A. S., Bemmel I. M. v., Röttgering H. J. A., 2009, *Astronomy & Astrophysics*, 501, 1185
- Intema H. T., Weeren R. J. v., Röttgering H. J. A., Lal D. V., 2011, *Astronomy & Astrophysics*, 535, A38
- Intema H. T., Jagannathan P., Mooley K. P., Frail D. A., 2017, *Astronomy & Astrophysics*, Volume 598, id.A78, 598, A78
- Jackson N., et al., 2016, *Astronomy & Astrophysics*, 595, A86
- Jackson N., et al., 2022, *Astronomy & Astrophysics*, 658, A2
- Jannuzi B. T., Dey A., 1999, The NOAO Deep Wide-Field Survey, <https://ui.adsabs.harvard.edu/abs/1999ASPC...193..258J>
- Jarvis M. E., et al., 2019, *Monthly Notices of the Royal Astronomical Society*, 485, 2710
- Jarvis M. E., et al., 2021, *Monthly Notices of the Royal Astronomical Society*, 503, 1780
- Jong J. M. G. H. J. d., et al., 2025, Scalable and robust wide-field facet calibration with LOFAR's longest baselines, doi:10.48550/arXiv.2508.12115, <http://arxiv.org/abs/2508.12115>
- Jurlin N., Brienza M., Morganti R., Wadadekar Y., Ishwara-Chandra C. H., Maddox N., Mahatma V., 2021, *Astronomy & Astrophysics*, 653, A110
- Kharb P., Subramanian S., Das M., Vaddi S., Paragi Z., 2021, *The Astrophysical Journal*, 919, 108
- Klein U., Lisenfeld U., Verley S., 2018, *Astronomy & Astrophysics*, 611, A55
- Kondapally R., et al., 2021, *Astronomy & Astrophysics*, 648, A3
- Kormendy J., Richstone D., 1992, *The Astrophysical Journal*, 393, 559
- Kormendy J., Richstone D., 1995, *Annual Review of Astronomy and Astrophysics*, 33, 581
- Kravchenko E. V., Pashchenko I. N., Homan D. C., Kovalev Y. Y., Lister M. L., Pushkarev A. B., Ros E., Savolainen T., 2025, *Monthly Notices of the Royal Astronomical Society*, 538, 2008
- Kreuzinger M., et al., 2024, *Astronomy & Astrophysics*, 690, A321
- Kukreti P., Morganti R., 2024, Connecting the radio AGN life cycle to feedback: Ionised gas is more disturbed in young radio AGN, <http://arxiv.org/abs/2407.06265>
- Kukreti P., Morganti R., Tadhunter C., Santoro F., 2023, *Astronomy & Astrophysics*, 674, A198
- Kukreti P., Wylezalek D., Albán M., Dall'Agnol de Oliveira B., 2025, *Astronomy and Astrophysics*, 698, A99
- Lacy M., et al., 2020, *Publications of the Astronomical Society of the Pacific*, 132, 035001
- Laor A., Behar E., 2008, *Monthly Notices of the Royal Astronomical Society*, 390, 847
- Lister M. L., Homan D. C., 2005, *The Astronomical Journal*, 130, 1389
- Liu H.-Y., Liu W.-J., Dong X.-B., Zhou H., Wang T., Lu H., Yuan W., 2019, *The Astrophysical Journal Supplement Series*, 243, 21
- Lonsdale C. J., et al., 2003, SWIRE: The SIRTf Wide-Area Infrared Extragalactic Survey
- Lyke B. W., et al., 2020, *The Astrophysical Journal Supplement Series*, 250, 8
- Magorrian J., et al., 1998, *The Astronomical Journal*, 115, 2285
- Maini A., Prandoni I., Norris R. P., Giovannini G., Spitler L. R., 2016, *Astronomy & Astrophysics*, 589, L3
- Meenakshi M., et al., 2022, *Monthly Notices of the Royal Astronomical Society*, 516, 766
- Meenakshi M., Mukherjee D., Bodo G., Rossi P., Harrison C. M., 2024, A comparative study of radio signatures from winds and jets: Modelling synchrotron emission and polarization, doi:10.48550/arXiv.2408.00099, <http://arxiv.org/abs/2408.00099>
- Merritt D., Ferrarese L., 2001, *The Astrophysical Journal*, 547, 140
- Miley G., 1980, *Annual Review of Astronomy and Astrophysics*, 18, 165
- Moldón J., et al., 2015, *Astronomy & Astrophysics*, 574, A73
- Molyneux S. J., Harrison C. M., Jarvis M. E., 2019, *Astronomy & Astrophysics*, 631, A132
- Morabito L. K., et al., 2022a, Identifying active galactic nuclei via brightness temperature with sub-arcsecond International LOFAR Telescope observations, doi:10.48550/arXiv.2207.13096, <http://arxiv.org/abs/2207.13096>
- Morabito L. K., et al., 2022b, *Astronomy & Astrophysics*, 658, A1
- Morabito L. K., et al., 2025a, *Astrophysics and Space Science*, 370, 19
- Morabito L. K., et al., 2025b, *Monthly Notices of the Royal Astronomical Society: Letters*, 536, L32
- Mullaney J. R., Alexander D. M., Fine S., Goulding A. D., Harrison C. M., Hickox R. C., 2013, *Monthly Notices of the Royal Astronomical Society*, 433, 622
- Nesvadba N. P. H., Drouart G., Breuck C. D., Best P., Seymour N., Vernet J., 2017, *Astronomy & Astrophysics*, 600, A121
- Njeri A., et al., 2025, The Quasar Feedback Survey: zooming into the origin of radio emission with e-MERLIN, doi:10.1093/mnras/staf020, <http://arxiv.org/abs/2501.03433>
- Offringa A. R., 2010, *Astrophysics Source Code Library*, p. ascl:1010.017
- Offringa A. R., et al., 2014, *Monthly Notices of the Royal Astronomical Society*, 444, 606
- Padovani P., 2016, *The Astronomy and Astrophysics Review*, 24, 13
- Panessa F., Giroletti M., 2013, *Monthly Notices of the Royal Astronomical Society*, 432, 1138
- Panessa F., Baldi R. D., Laor A., Padovani P., Behar E., McHardy I., 2019, *Nature Astronomy*, 3, 387
- Petley J. W., et al., 2022, *Monthly Notices of the Royal Astronomical Society*, 515, 5159
- Pötzl F. M., et al., 2021, *Astronomy & Astrophysics*, 648, A82
- Rawlings S., Saunders R., Eales S. A., Mackay C. D., 1989, *Monthly Notices of the Royal Astronomical Society*, 240, 701
- Richards G. T., et al., 2006, *The Astrophysical Journal Supplement Series*, 166, 470
- Rubeis E. D., et al., 2025, Revealing the intricacies of radio galaxies and filaments in the merging galaxy cluster Abell 2255. I. Insights from deep LOFAR-VLBI sub-arcsecond resolution images, doi:10.48550/arXiv.2505.13595, <http://arxiv.org/abs/2505.13595>
- Rubeis E., et al., 2026, *Astronomy & Astrophysics*
- Sabater J., et al., 2021, *Astronomy & Astrophysics*, 648, A2
- Scaife A. M. M., Heald G. H., 2012, *Monthly Notices of the Royal Astronomical Society: Letters*, 423, L30
- Scholtz J., et al., 2021, *Monthly Notices of the Royal Astronomical Society*, 505, 5469
- Shimwell T. W., et al., 2017, *Astronomy & Astrophysics*, 598, A104
- Shimwell T. W., et al., 2019, *Astronomy & Astrophysics*, 622, A1
- Shimwell T. W., et al., 2022, *Astronomy & Astrophysics*, 659, A1
- Shimwell T. W., et al., 2025, *Astronomy & Astrophysics*, 695, A80
- Smith D. J. B., et al., 2016, The WEAVE-LOFAR Survey, doi:10.48550/arXiv.1611.02706, <http://arxiv.org/abs/1611.02706>
- Speranza G., et al., 2024, *Astronomy and Astrophysics*, 681, A63
- Sweijen F., et al., 2022, *Nature Astronomy*, 6, 350
- Tabatabaei F. S., et al., 2013, *Astronomy & Astrophysics*, 552, A19
- Tasse C., et al., 2021, *Astronomy & Astrophysics*, 648, A1
- Veilleux S., Maiolino R., Bolatto A. D., Aalto S., 2020, *Astronomy and Astrophysics Review*, 28, 2
- Venturi G., et al., 2021, *Astronomy and Astrophysics*, 648, A17
- Vries W. H. d., Hodge J. A., Becker R. H., White R. L., Helfand D. J., 2007, *The Astronomical Journal*, 134, 457
- Walter F., Brinks E., de Blok W. J. G., Bigiel F., Kennicutt R. C., Thornley M. D., Leroy A., 2008, *The Astronomical Journal*, 136, 2563

- Ward S. R., Costa T., Harrison C. M., Mainieri V., 2024, AGN-driven outflows in clumpy media: multiphase structure and scaling relations, doi:10.48550/arXiv.2407.17593, <http://arxiv.org/abs/2407.17593>
- Weeren R. J. v., et al., 2016, *The Astrophysical Journal Supplement Series*, 223, 2
- Ye H., et al., 2024, *Astronomy & Astrophysics*, 691, A347
- Zakamska N. L., Greene J. E., 2014, *Monthly Notices of the Royal Astronomical Society*, 442, 784
- Zakamska N. L., et al., 2016, *Monthly Notices of the Royal Astronomical Society*, 459, 3144
- de Gasperin F., et al., 2019, *Astronomy & Astrophysics*, 622, A5
- de Jong J. M. G. H. J., et al., 2024, Into the depths: Unveiling ELAIS-N1 with LOFAR's deepest sub-arcsecond wide-field images, <http://arxiv.org/abs/2407.13247>
- van Diepen G., Dijkema T. J., Offringa A., 2018, *Astrophysics Source Code Library*, p. ascl:1804.003
- van Weeren R. J., et al., 2021, *Astronomy and Astrophysics*, 651, A115

APPENDIX A: ILT WIDE-FIELD DATA REDUCTION DETAILS

In this appendix, we discuss the data reduction techniques we implement to obtain the Boötes high-resolution, wide-field images. All the scripts we discuss in the following sections are integrated into the publicly available pipeline (van der Wild et al. in prep)⁶.

Before the observation becomes available on the LTA, some pre-processing is required. Any time periods or frequencies affected by Radio Frequency Interference (RFI) are flagged using AOFlogger⁷ (Offringa 2010). The first and last channels were flagged, as their edges contain various imperfections that can degrade data quality. The data was then averaged to 16 channels per subband with a frequency of 12.21 kHz per channel in order to reduce data volume and this averaged data is then uploaded to the LTA.

We note that the data reduction steps below are now being automated in the publicly available pipeline (van der Wild et al. in prep., Jong et al. 2025). We conducted these steps manually as the automated pipeline development was in early stages at the start of data processing for Boötes.

The second stage of reducing our Boötes LTA pointing uses the PREFACTOR⁸ pipeline which is split into two parts, Pre-Facet-Calibrator and Pre-Facet-Target. PREFACTOR is now deprecated and users should now turn to LINC⁹, but this was not fully operational at the time of processing.

A0.1 Pre-Facet-Calibrator

The first step of running the PREFACTOR pipeline is running Pre-Facet-Calibrator which considers all stations, both Dutch and international. Here, we derive corrections for the DIEs, namely polarisation offset, bandpass, and clock offset.

This section of the pipeline uses a bright 3C source that was specifically specified for the particular observation and uses this 3C source as a flux calibrator. These sources have a known radio spectrum, morphology, and are unpolarised at 144 MHz (Scaife &

Heald 2012). For this 8-h observation of Boötes the flux calibrator source was 3C 196.

A0.2 Pre-Facet-Target

After we run Pre-Facet-Calibrator, the solutions from the flux calibrator are applied to the target observation of the Dutch stations only and hence dramatically reduces the data volume. We then apply the calibrator solutions to the target data for the polarisation alignment, bandpass, clock offset, and finally, a beam correction. If required, bright off-axis sources are removed from the target observation during the A-Team clipping step, where the four brightest radio sources in the northern hemisphere (the supernova remnants Cassiopeia A and Taurus A, and the radio galaxies Cygnus A and Virgo A) are flagged if their emission exceeds a certain threshold and they are in close proximity to the centre of the observation. Then, we further average the data to 8 seconds and 97.64 KHz. We also apply a coarse rotation measure correction based on Global Position System (GPS) information alongside the flux calibrator solutions. The final step of Pre-Facet-Target is to perform a direction independent phase-only calibration, only on the Dutch stations, using a skymodel from TGSS (Tata Institute of Fundamental Research (TIFR) Giant Metrewave Radio Telescope (GMRT) Sky Survey; Intema et al. 2017). This provides an initial direction independent correction for ionospheric effects. Finally, these corrections are applied to the measurement sets, producing DIE corrected data sets.

A0.3 Source Subtraction Outside the International FoV

When incorporating the international stations into the data reduction process, we significantly reduce our FoV. This is because the international stations of the ILT are physically larger in size than the Dutch core and remote stations, therefore the beams of the international stations are smaller in comparison to the beam of the Dutch stations. We therefore subtract sources from the uv data that are outside of the international station FoV.

We run the DDF pipeline¹⁰, which provides both DDE and DIE solutions for the Dutch stations. We took the 6'' resolution image which we produce during our run of the DDF pipeline and we ran sub-sources-outside-region.py¹¹. We subtracted sources outside of a 2.5×2.5 deg² box region which represents the international FoV. This step is taken to prevent areas of the sky visible only to the Dutch stations, and not to the international ones, from affecting calibration and imaging, especially in the presence of bright sources.

A0.4 In-field Calibration

The next stage of data processing is using the LOFAR-VLBI pipeline. As a first step it performs a bulk DIE correction for the international stations, using the best in-field delay calibrator within the FoV of the international stations. We apply the solutions we produce using this in-field calibrator to both the Dutch and international stations. This is a critical part of reducing any ILT pointing because once the solutions from the in-field calibrator have been applied, calibration errors introduced at this stage are difficult to correct for, due

⁶ VLBI Github repository: <https://git.astron.nl/RD/VLBI-cwl>

⁷ AOFlogger: <https://aoflogger.readthedocs.io/en/latest/>

⁸ The PREFACTOR pipeline is publicly available at: <https://github.com/lofar-astron/prefactor>

⁹ LINC is publicly available at: <https://git.astron.nl/RD/LINC>.

¹⁰ The DDF pipeline is publicly available at: <https://github.com/mhardcastle/ddf-pipeline>

¹¹ sub-sources-outside-region.py script is publicly available: https://github.com/rvweeren/lofar_facet_selfcal/blob/main/submods/sub_sources_outside_region.py

to the use of small time and frequency solution intervals. Before we select a calibrator, we first apply the DI solutions from both Pre-Facet-Calibrator (Section A0.1) and Pre-Facet-Target (Section A0.2). Then we separate the data into 24 manageable measurements sets, each with ~ 2 MHz bandwidth. During this process, we produce a list of potential LBCS (LOFAR Long-Baseline Calibrator Survey; Moldón et al. 2015; Jackson et al. 2016, 2022) sources. This catalogue contains potential in-field calibrator sources, taking into account the brightness of these sources at $6''$ and the position relative to the pointing centre. The ideal in-field calibrator source is compact and bright at $0.3''$ while being within the international station FWHM. At this stage of the data reduction process, the source's morphology at $0.3''$ is not known. Therefore, the source ranked as the most likely best in-field calibrator in the LBCS catalogue may not be the best one, and hence we verify the LBCS selection. The previous pipeline version selected the LBCS calibrator with compact flux and was closest to the pointing centre, however, these two criteria alone are insufficient for identifying a suitable in-field calibrator. Consequently, we process multiple candidate calibrators during data reduction. We then split out these potential in-field calibrators from the field and calibrate them individually to determine which source is the best calibrator within the FoV.

To determine whether the sources which we select using LBCS are suitable in-field calibrators, we conduct self-calibration of these sources. The aim of self-calibration is to find the complex gains which we require to reproduce the sky intensity model given the visibilities observed. To do this, an initial model is created and the complex gains are then solved for and the corrected visibility is calculated. Using this corrected visibility, a new and improved model is formed. We repeat this process until the model created is representative of the observed source. We implement `facetselfcal` (van Weeren et al. 2021) to perform all self-calibration procedures to create these Boötes images. This software uses the default preprocessing pipeline (DP3; van Diepen et al. (2018)) to calculate complex gains and `WSClean` (Offringa et al. 2014) for imaging. For our potential calibrator sources we set the number of self-calibration cycles to 10, as this generally leads to convergence (e.g. Sweijen et al. 2022; Ye et al. 2024).

For this Boötes pointing, we reduce two LBCS sources to sub-arcsecond resolution, both of which are double sources at $0.3''$. Of the two, we chose ILTJ142905.10+342641.0 as the in-field calibrator because the calibration solutions are cleaner compared to the first source, and this source is closer to the pointing centre of the observation. This highlights the importance of considering multiple sources as potential in-field calibrators.

We applied the calibrator solutions which we produced from the self-calibration of the in-field calibrator to the subtracted measurement set. For this step, we phase-shift toward our in-field calibrator and form a "super station" (ST001) where we combine all the core stations to reduce the data volume, increase SNR, and suppress signals from other sources due to the reduced FoV.

A1 Direction Dependent Calibrators

The solutions we apply from the in-field calibrator only provide corrections in the direction of the in-field calibrator, leaving residual DDEs that still require correcting. For wide-field imaging using the ILT, we require multiple calibrator sources across our FoV referred to as DDCs (Directional Dependent Calibrators) to correct for the residual DDEs.

The ideal candidates for these DDCs are the same as our selection of an in-field calibrator where high brightness and compactness are

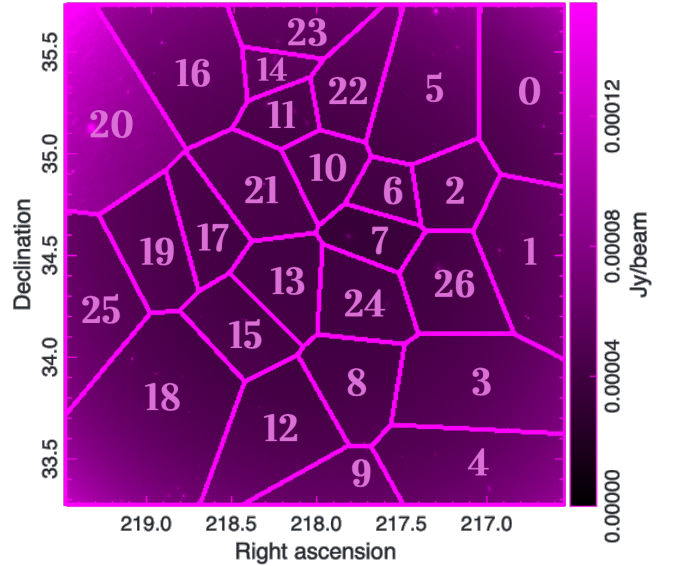


Figure A1. The layout of the 27 facets we use to produce the sub-arcsecond resolution, wide-field, images of the Boötes Deep Field. The background is the $\sim 0.3''$ RMS image and facet 20 has a higher level of noise due to an extra flux scaling correction required for this facet.

desirable. Unfortunately, at such high-resolution, these sources are rare. Therefore, we must loosen our requirements to obtain the best understanding of ionospheric conditions across our FoV. We do not have to be as strict with our selection of DDCs compared to the selection of our in-field calibrator, as our in-field calibrator has corrected for the bulk of distortions. We consequently include fainter and extended sources within our selection of these DDCs, as long as these objects' calibration solutions converge through the self-calibration cycles.

For this field we select 26 DDCs and hence have 27 directions in total within our field, including the in-field calibrator. To begin this selection, we consider sources identified as potential in-field calibrators, but ultimately do not adopt them as the in-field calibrator. We also consider the next 100 brightest objects in the $6''$ image that lie within the international FoV. Therefore, we choose our DDCs from 112 sources. We split each of these sources from the field and then conduct self-calibration on each of them individually to determine if they are a suitable DDC. We then visually inspect the resulting images and solutions to determine their suitability.

Now that we have our DDCs, we split the field into facets using Voronoi tessellation (e.g. Weeren et al. 2016), which sets the dimensions of each facet by assigning every point in the plane to its nearest calibrator source such that each facet contains all points closer to that calibrator than to any other. This results in the non-symmetric facets and from this step forward we consider each facet individually rather than the entire FoV. We demonstrate the facet layout for the sub-arcsecond resolution Boötes images in Figure A1, and we note that facet 20 has higher noise in comparison to other directions which is further described in Section A2.1.

A2 High-Resolution Imaging

The first image we create of Boötes (using `WSClean`) is at $\sim 1.2''$ resolution. We produce this image first to check the quality of the calibration of the image because of its comparatively low computa-

tional cost. This 1.2'' image was imaged in one go using WSClean's facet mode, however this is not possible for the 0.6'' and 0.3'' images. Instead, the 1.2'' model images were used to create individual datasets for each facet (refer to Figure A1 for facet layout) which could then be imaged independently, allowing for faster and less computationally expensive sub-arcsecond imaging.

To create the individual datasets for each of these facets, we first subtract all sources within the field and using the `-predict` functionality of WSClean and the 1.2'' model images. We then add back the sources within the facet using the solutions of the corresponding DDCs, hence giving calibrated datasets for each facet. We complete this for each of the 27 facets, and are left with 27 facet images. We do this independently for the 0.3'' and 0.6'' images.

The final step is to mosaic these facets together using SWarp¹² (Bertin et al. 2002) to create the final image at 0.3'' (which we show in Figure 2), as well as the final 0.6'' image.

A2.1 Flux Density Scale and Astrometry Corrections

The self-calibration which we implement to create these images is agnostic to the position of sources when there is not a reference source, therefore, the resulting images contain both an astrometry and flux density offset. These offsets are introduced by the delay calibrator rather than our DDCs, as during self-calibration of our DDCs we normalise the amplitudes to minimise any drift in the flux scale. A position shift may also be present because for Boötes, we do not have an astrometric reference for the delay calibrator selected. Similarly, although the amplitude scale was tied to archival data, residual offsets from the desired flux density scale may remain, so the source flux densities require scaling to match to known flux density measurements within the literature. To derive these corrections, we locate compact, high SNR, sources using a compactness measurement from the peak intensity and total flux intensity from Kondapally et al. (2021) as well as the respective high-resolution images from pyBDSF¹³. For flux scaling, we apply a universal correction across all facets, by taking the median flux scaling of all facets combined (due to the substantial uncertainties in the flux scaling for the ILT) and we perform the astrometry correction for each facet individually. We apply the correction calculated for the 0.3'' image for each resolution as both the astrometry and flux scaling offset is not dependent on the resolution as we create each resolution image using the same dataset.

To determine the flux scaling we require, we use the total flux density measurements at 6'' and compare this to the measurement of flux density at 0.3''. For this correction we consider sources with $S_{\text{peak}}/S_{\text{total}} > 0.7$ and from these sources, we use a SNR cut off of 10 using the peak intensity measurement and the RMS (root mean squared) island noise from the 0.3'' image. This leaves 343 sources at 0.3''. We incorporate an initial universal flux scaling correction of 1.111 to the high-resolution images. We investigate the scatter in the flux scaling correction between facets to determine the uncertainties in this flux scale correction. We fit a Gaussian to the flux scaling correction distribution and adopt the standard deviation of the fit, 24.8 per cent, as the uncertainty in the flux scaling. For Boötes we add a further flux scale to correct for flux measurement deviations between the LoTSS Deep 6'' image and a 6'' image produced with this data set and calibration methods. To do this, we locate sources in LoTSS with SNR greater than 20 with $S_{\text{peak}}/S_{\text{total}} > 0.9$, leaving 990 sources. Using the flux density measurements from LoTSS Deep

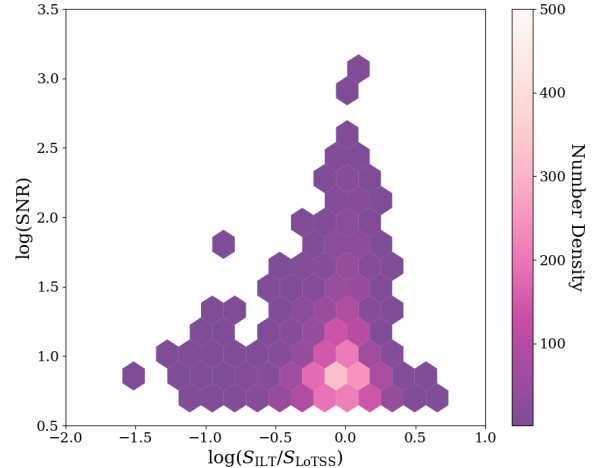


Figure A2. The SNR of the $\sim 0.3''$ resolution image as a function of the ratio between the flux density at 0.3'' (S_{ILT}) and flux density at 6'' (S_{LoTSS}), where we trace the number density with the colour bar. For a hexagon to be plotted, at least 2 sources must lie within the bin.

and the new 6'' image, we find a flux scaling correction of 0.92. Combining this with our previous flux scaling correction, for the whole field we incorporate a flux scale of 1.02.

To correct for the astrometric offset, we use the RA and DEC of the optical counterparts from Kondapally et al. (2021) to calculate the offsets between the LoTSS Deep 6'' catalogue and the 0.3'' resolution image. Our definition for compact sources is more lenient for the position offset as we correct per facet for this offset rather than a universal correction and therefore prioritise count statistics per facet. We reduce our criteria to $S_{\text{peak}}/S_{\text{total}} > 0.6$ followed by a SNR cut off of 7. This leaves 954 sources, with the largest number of compact sources in a single facet of 80 and a smallest of 3. We correct the astrometry per facet by taking the median RA and DEC offset in each facet. The RA correction ranges from 0.0982'' to 0.576'' with an overall median of 0.319'' and the DEC correction ranges from -0.425'' to 0.289'' with a median of 0.0367''.

The astrometry correction in the images for Boötes is larger than that of the ELAIS-N1 field. The key reason for this is that the in-field calibrator source for ELAIS-N1 has a high frequency VLBI position based on Charlot et al. (2020). Therefore for this field the authors could achieve millisecond accuracy for the positioning of this source. For future fields that are to be reduced at sub-arcsecond scale, it is important to consider the astrometry early on and potentially select calibrators that have a highly accurate position available.

We note that facet 20 had relatively poor calibration in comparison to other facets within this image. Therefore, we apply a further flux scaling correction to this facet using the same method as above. In Figure A1 we can see this has higher noise in comparison to the other facets.

A2.2 Catalogue Construction and Component Association

We produce the final catalogues, corrected for astrometry and flux scale, for each of the three resolution images using pyBDSF with a pixel detection threshold of 5σ and a detection island threshold of 3σ , an RMS box of (120,15), and for bright-source RMS box of

¹² SWarp is publicly available at: <https://ascl.net/1010.068>

¹³ <https://pybdsf.readthedocs.io/en/latest/>

(40,15) following de Jong et al. (2024). For the 0.3'', 0.6'', and 1.2'' catalogues we detect 8048, 5851, and 2596 components respectively at 5σ .

In the published source catalogues, the components have been associated in several stages. If a single component at the relevant high-resolution image is isolated within the 6'' beam of the LoTSS Deep Field image, we class it as a single component source. At 0.3'' if multiple components are present within a separation 30'' of each other, we perform visual inspection to check if components should be associated to a common source, by creating a 60'' \times 60'' cutout. These cutouts also have information at other resolutions to allow simultaneous component association at each resolution. For instance, 6'' resolution images allow us to de-blend sources, which could be confused as multiple components for a single source rather than multiple sources. For a handful of cases, we require further information to determine whether components are blended sources rather than a single source. In these cases we consult the NOAO Deep Wide Field Survey (NDWFS; Jannuzi & Dey 1999) optical image of Boötes at I-band to either keep components separate or associate these components. Using a separation of 30'' misses giant radio galaxies within our images, therefore we also use the LOFAR Galaxy Zoo (LGZ) within Kondapally et al. (2021) to visually inspect sources with a LGZ size greater than 30''.

These methods result in a total of 585 components being merged into 223 sources at 0.3''. At 0.6'' 434 components are merged into 152 sources, and finally at 1.2'' 166 components are merged to 65 sources.

When merging sources, we sum the total flux density of all components and perform standard error propagation on their errors. We take the mean of the island RMS noise levels as a proxy for the local RMS noise of the associated source. We take the highest peak intensity value alongside the associated error. The RA and DEC for these sources is the flux density weighted position. Finally we calculate the Largest Angular Size (LAS) for these sources, by considering each component's major and minor axes, as well as their respective position angle. We set the major and minor axes and the position angle of these sources to zero in the catalogue. We obtain the uncertainties for the LAS by using the uncertainty extremities of the major and minor axis, as well as the position angle.

During the visual inspection of sources, several of the components within a certain separation appeared to be artifacts. We remove these from our final catalogues. For 0.3'' we remove 69 components, 45 at 0.6'' and 4 at 1.2''.

Many false detections are present within the initial pyBDSF catalogues. The 6'' image of Boötes from LoTSS is deeper than the images presented in this paper and therefore can be used to help identify false detections. To remove these false detections, firstly we located sources which do not lie within 3'' of a LoTSS source, as sources within this radius would be associated to the LoTSS 6'' source. We only consider sources with a flux density below 500 μ Jy measured at the given high-resolution image because sources below this threshold are where we expect to start to see false detections. We then measure the median 5σ RMS noise within a 3'' radius region of the LoTSS position in the RMS map¹⁴. If the flux density in the high-resolution image of the source is greater than the 5σ median RMS at 6'' then we class this as a false detection and remove this from our final catalogue. However, if the flux density is less than the 5σ median RMS then this is a possible real detection that was not

detected at 6''. We remove 3541 false detections at 0.3'' with 278 potential new detections, at 0.6'' we remove 1070 false detections and have 13 new detections, and at 1.2'' we remove 10 detections and have no new detections at this resolution.

Finally, we conduct one final round of visual inspection of the whole field to ensure the brightest sources have been correctly associated. In the 0.3'' image we associate four components into two sources and in the 1.2'' we associate three components into one source. This leaves us with the final catalogue at each resolution. The 0.3'' catalogue contains 4074 sources, 4455 at 0.6'', and 2480 at 1.2''. We note that the highest source count of the three resolution images released in this paper is in the \sim 0.6'' resolution image. This is because at the highest resolution, 0.3'', we are probing the smallest scale emission at this frequency, therefore as we decrease resolution we increase sensitivity to lower surface brightness emission and we are more likely to detect diffuse emission on larger scales, and therefore at 0.6'' we can detect sources which cannot be detected at 0.3'' as these would be too diffuse. We do not however see the highest source count at the \sim 1.2'' image despite this being the lowest resolution as this image has the lowest sensitivity due to gaps in the uv coverage.

Figure A2 shows us how the ratio of flux density at 0.3'' (S_{ILT}) and flux density at 6'' (S_{LoTSS}) varies with SNR which we measure from the 0.3'' image by taking the ratio of peak intensity and flux densities as measured by pyBDSF. The sources contributing to this figure are detected within 1'' of their LoTSS position. As expected, we see the majority of sources lie at low SNR and have a logarithmic ratio of (S_{ILT}) and (S_{LoTSS}) slightly below zero, as we expect some emission to be resolved out when we increase the length of our baselines. We do see some sources which lie above zero, and this appears to occur at a lower SNR ratio. This happens as at lower SNR it becomes increasingly difficult for pyBDSF to measure flux density and hence the fluxes maybe overestimated, because not all the flux detected is associated with the source, and is likely to be a noise contribution.

APPENDIX B: [O III] KINEMATICS

To further investigate the relationship between [O III] and high-resolution radio morphologies, we investigate how [O III] kinematics (derived from Escott et al. 2025) vary depending on whether a source is detected or undetected at 0.3'' using cumulative distribution functions (CDFs). Here, we are not investigating the variation between AGN with [O III] outflows and AGN with no [O III] outflows, and therefore we do not use the $L_{6\mu m}$ and redshift matched population. We check that the 2D KS test for $L_{6\mu m}$ and redshift between the detected and undetected populations outputs a p value above 0.05, and therefore these two populations can be compared without matching being necessary. We note that we do not draw any significant conclusions from these CDFs due to our limited sample size as the detected population has 35 AGN and the undetected have 41 AGN.

Figure B1 and Figure B2 illustrates the relationship between two kinematics properties of [O III] and how they vary depending on if they are detected at sub-arcsecond resolution or not. Detected AGN are depicted with purple solid lines, and we show undetected AGN with dashed pink lines. Figure B1 shows the results for the integrated flux of the broad component of [O III] which we define as the area of the component which we calculate using the peak and FWHM of the broad Gaussian component. Only AGN which are within the [O III] fitted outflow category are included as we require a broad component to be present. We see a higher integrated flux of the broad component

¹⁴ The RMS map is available at: https://lofar-surveys.org/deepfields_public_bootes.html

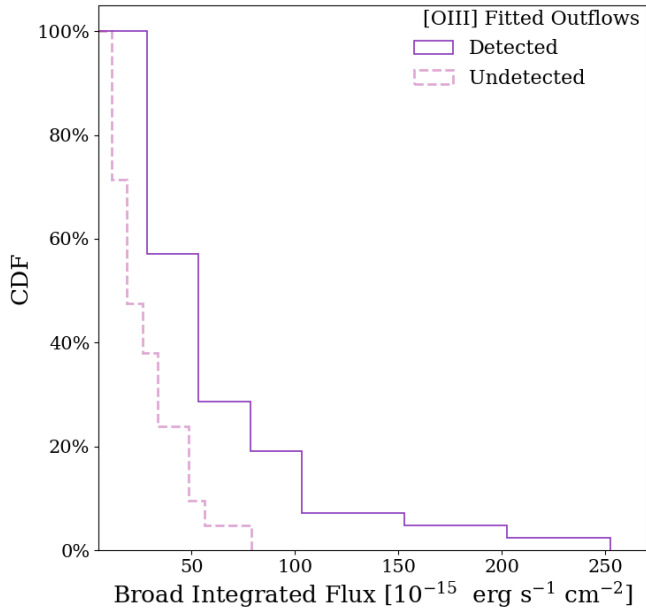


Figure B1. Cumulative Distribution Function AGN with an [O III] fitted outflow comparing the integrated flux of the broad component fitted to [O III] of detected and undetected AGN at $0.3''$. The solid purple histograms show the results for the detected AGN and the dashed pink histogram portrays the undetected AGN.

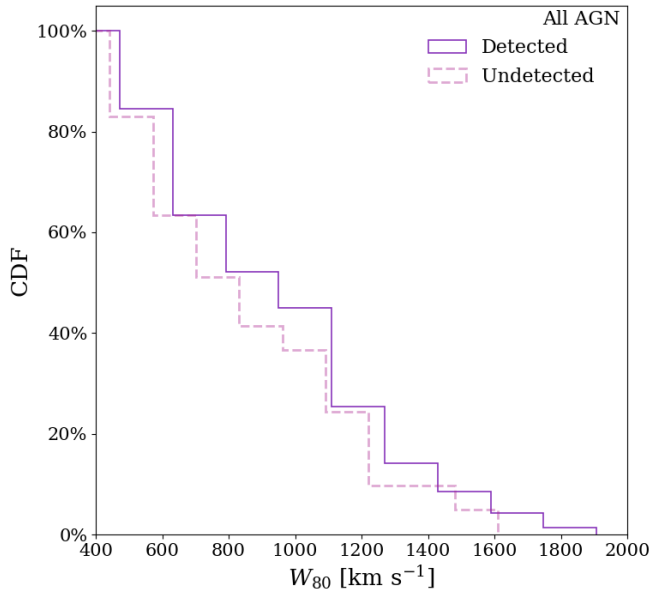


Figure B2. Cumulative Distribution Function all AGN, regardless of [O III] outflow type comparing the W_{80} of detected and undetected AGN at $0.3''$. The solid purple histograms show the results for the detected AGN and the dashed pink histogram portrays the undetected AGN.

when the AGN are detected compared to AGN which are undetected at $0.3''$.

Figure B2 compares how the W_{80} varies between the two populations. Again, here we see that compact AGN have a larger W_{80} (which is a non-parametric proxy) compared to the undetected AGN, however this is at a lesser extent in comparison to the increase we see in the integrated flux of the broad component.

Both these CDFs show similar results to the kinematic analysis in Escott et al. (2025) where the authors compare these kinematics between AGN detected at $6''$ and AGN not detected at $6''$, whereas in this work, we are comparing AGN which are all detected at $6''$, but the detected AGN are still detected at $0.3''$ and the undetected population are not detected at $0.3''$. As we still see the enhanced kinematics of [O III] in the detected population at $0.3''$, this suggests that the relation is not driven by the emission which is resolved out in-between $6''$ and $0.3''$. Due to our limited sample size and lack of uncertainties, we require larger samples in further work to probe the concreteness of this result.

This paper has been typeset from a \LaTeX file prepared by the author.